

## **Distribution Agreement**

In presenting this thesis as a partial fulfillment of the requirements for a degree from Emory University, I hereby grant to Emory University and its agents the non-exclusive license to archive, make accessible, and display my thesis in whole or in part in all forms of media, now or hereafter now, including display on the World Wide Web. I understand that I may select some access restrictions as part of the online submission of this thesis. I retain all ownership rights to the copyright of the thesis. I also retain the right to use in future works (such as articles or books) all or part of this thesis.

Saitheja Pucha

April 2, 2025

Microenvironmental Guidance of Early Cell Mechanoreponse and Precise Matrix Deposition for  
Meniscus Tissue Engineering

by

Saitheja Pucha

Jay Patel  
Adviser

Department of Biology

Dr. Jay Patel  
Adviser

Dr. Megan Cole  
Committee Member

Dr. Miguel Reyes  
Committee Member

2025

Microenvironmental Guidance of Early Cell Mechanoreponse and Precise Matrix Deposition for  
Meniscus Tissue Engineering

By

Saitheja Pucha

Dr. Jay Patel  
Adviser

An abstract of  
a thesis submitted to the Faculty of Emory College of Arts and Sciences  
of Emory University in partial fulfillment  
of the requirements of the degree of  
Bachelor of Science with Honors

Department of Biology

2025

## Abstract

### Microenvironmental Guidance of Early Cell Mechanoresponse and Precise Matrix Deposition for Meniscus Tissue Engineering By Saitheja Pucha

The meniscus is a fibrocartilaginous structure in the knee joint that plays a crucial role in load distribution, shock absorption, and joint stability. Meniscus injuries are a significant orthopaedic challenge, often leading to joint degeneration and osteoarthritis. While tissue-engineered scaffolds show promise for meniscal regeneration, understanding early cellular responses to biomaterial environments remains crucial for optimizing scaffold design. Additionally, the spatial heterogeneity of meniscal extracellular matrix (ECM) is crucial to recapitulating the native function of the tissue. This study investigates how 3D hydrogel microenvironments influence early cell mechanoresponse and ECM deposition, focusing on marrow stromal cells (MSCs) and meniscal fibrochondrocytes (MFCs), for the eventual goal of optimizing the design of tissue-engineered meniscus scaffolds.

Using fibrin-based hydrogels, we fabricated fiber-reinforced microenvironments that emulate the mechanical anisotropy of native meniscus tissue. MSCs encapsulated within fiber-reinforced constructs exhibited heterogeneous morphological and mechanosensitive responses, which were analyzed using principal component analysis (PCA) and agglomerative hierarchical clustering (AHC). This approach identified three distinct cell subpopulations based on cell morphology and nuclear translocation of YAP, a key mechanotransduction marker. Notably, high-response MSCs preferentially localized near stiff polymer fibers, suggesting a distance-dependent mechanosensitive response.

To further explore early cell-matrix interactions, we used methacrylated gelatin and hyaluronic acid hydrogels (GelMA/MeHA) to investigate microenvironmental influence of nascent ECM production by MFCs. It was found that MFCs possess an inherent ability to deposit aligned matrix within 14 days, and increasing MeHA content in GelMA hydrogels suppressed matrix anisotropy, demonstrating that biomaterial composition directly influences meniscal ECM organization. Various GelMA/MeHA formulations promoted differential distributions of protein and glycosaminoglycan (GAG) deposition by MFCs within 3 days, providing a promising avenue by which to precisely guide ECM deposition in tissue engineered meniscus.

Overall, this study provides novel insights into early cell-matrix interactions in meniscal tissue engineering. By identifying spatially responsive cell populations and their mechanosensitive behaviors, we establish a framework for optimizing fiber-reinforced scaffolds. These findings contribute to the design of next-generation meniscus replacements that control cellular guidance and ECM deposition. Future studies will focus on integrating these biomaterial strategies into preclinical models to assess long-term tissue maturation and biomechanical performance.

Microenvironmental Guidance of Early Cell Mechanoreponse and Precise Matrix Deposition for  
Meniscus Tissue Engineering

By

Saitheja Pucha

Dr. Jay Patel  
Adviser

A thesis submitted to the Faculty of Emory College of Arts and Sciences  
of Emory University in partial fulfillment  
of the requirements of the degree of  
Bachelor of Science with Honors

Department of Biology

2025

## Acknowledgements

I would like to thank the Atlanta Veterans Affairs Medical Center, the department of Orthopaedics at Emory University, and all members of the Patel Lab for their contributions to this research.

\*\*Note: Areas of Introduction (p.1-6, Cell Preparation, Culture, and Native Meniscus Sectioning (p.7), Fibrin Gel Fabrication and Mechanical Testing (7-8), Cell Encapsulation and Hydrogel Culture – Fibrin Gels (p.8), Immunofluorescent Staining – Fibrin Gels (8-9), Image Acquisition and Cell Parameter Extraction – Fibrin Gels (p.9-10), Analysis Pipeline, PCA, AHC – Fibrin Gels (p.10-11), Figure 1 (p.15), Figure 4 (p.20), Figure 5 (p.21), Figure 6 (p.23), Figure 7 (p.24), Figure 8 (p.26), Figure 9 (p.28), and areas of Results/Discussion are directly taken from own published article.

Citation: Pucha, S. A., Hasson, M., Solomon, H., McColgan, G. E., Robinson, J. L., Vega, S. L., & Patel, J. M. (2024). Revealing Early Spatial Patterns of Cellular Responsivity in Fiber-Reinforced Microenvironments. *Tissue engineering. Part A*, 30(19-20), 614–626.  
<https://doi.org/10.1089/ten.TEA.2024.0017>

## Table of Contents

Introduction	1-6
Materials and Methods	7-18
<i>Cell Preparation, Culture, and Native Meniscus Sectioning</i>	7
<i>Fibrin Gel Fabrication and Mechanical Testing</i>	7-8
<i>Cell Encapsulation and Hydrogel Culture – Fibrin Gels</i>	8
<i>Immunofluorescent Staining – Fibrin Gels</i>	8-9
<i>Image Acquisition and Cell Parameter Extraction – Fibrin Gels</i>	9-10
<i>Analysis Pipeline, PCA, AHC – Fibrin Gels</i>	10-11
<i>Methacrylated Gelatin/Hyaluronic Acid Gel Fabrication</i>	11
<i>Nascent Matrix Labeling and Culture of GelMA/MeHA Hydrogels</i>	11-12
<i>Immunofluorescent Staining – GelMA/MeHA Gels</i>	12-13
<i>Imaging and Cell Parameter Extraction – GelMA/MeHA Gels</i>	13
<i>Pentanoate-Functionalized Hyaluronic Acid and Peptide Functionalization</i>	13-14
<i>Statistics</i>	17-18
Results	19-35
Discussion	36-40
Conclusions	41
References	42-51

## Table of Figures

Figure 1. Cell Feature Acquisition in Fiber-Reinforced Microenvironment.	15
Figure 2. Nascent Matrix Labeling of Meniscal Fibrochondrocytes.	16
Figure 3. Pentanoate-Functionalized HA MMP-Cleavable and RGD Peptide Functionalization.	17
Figure 4. Cell shape and nuclear response to a stiff polymeric fiber in a fiber-reinforced environment is highly heterogeneous.	20
Figure 5. Cell response to polymeric fiber is heightened in lower-stiffness (lower fibrinogen content) fibrin constructs.	21
Figure 6. A heterogeneous set of cells within a simulated fiber-reinforced hydrogel microenvironment can be clustered using Principal Component Analysis followed by Agglomerative Hierarchical Clustering.	23
Figure 7. Classification of acquired cell clusters based on cytoskeleton and nuclear response parameters.	24
Figure 8. Cell clusters localize differentially in fiber-reinforced micro-environment.	26
Figure 9. Stiffness of hydrogel substrate and fibrin remodeling capacity differentially influence level of morpho-mechanoresponse and spatial response of highly responsive cells in fiber-reinforced microenvironment.	28
Figure 10. Meniscus Anisotropy.	29
Figure 11. MFC Matrix Alignment Progression and Plasticity.	31
Figure 12. Microenvironment Impact on Matrix-Producing Phenotype.	33
Figure 13. Remodelability mediates Nascent Protein but not Nascent Gal deposition by MFCs.	35

## Introduction

The meniscus is a critical fibrocartilaginous disc-shaped tissue present within the knee joint essential for lubrication, load distribution, and overall joint stability<sup>1-3</sup>. The complex biomechanical functions of the meniscus are made possible by a heterogenous geometrical profile and extracellular matrix composition, with an inner zone consisting mostly of proteoglycans (PGs) and type II collagen and an outer zone composed of predominantly type I collagen organized in a circumferential manner<sup>4,5</sup>. However, due to the critical roles that the knee menisci play in daily motion and load-bearing, meniscus injury is very common; meniscus surgery is among the most common orthopaedic procedures conducted around the world<sup>6</sup>. Specifically, meniscal tears affect over 1 million people each year in the United States<sup>6</sup>. Damage to the meniscus leads to aberrant biomechanical function of the tissue in distributing load within the knee joint, causing increased contact pressures to the surrounding articular cartilage and an increased risk of osteoarthritis<sup>7</sup>. Currently, meniscectomy, a procedure by which damaged tissue is partially or totally resected, is the most relied upon treatment to manage pain and provide short-term symptomatic relief, with about 850,000 meniscectomies performed each year in the US<sup>8</sup>. Beyond this short-term relief, meniscectomy commonly results in aberrant joint distribution by the meniscus and an accelerated state of joint degeneration that leads to rapid onset of osteoarthritis in the joint<sup>9,10</sup>. Despite the perceived long-term functional benefits of opting to repair the meniscus rather than resecting the damaged portion, meniscectomies are performed at a far higher rate than meniscal repairs<sup>7,8,11</sup>. Meniscus tears, primarily radial tears, have little ability to self-heal primarily due to the relative avascularity of the tissue, especially the inner zone<sup>3</sup>. In addition to the lack of vascularity present throughout the meniscus, microenvironmental factors that inhibit effective restoration of the circumferentially oriented, anisotropic geometry of the matrix limit the extent to which the tissue can heal on its own; therefore, there remains a clinical need in the field for endogenous repair<sup>12</sup>.

Recently, tissue-engineered approaches to replace the meniscus by replicating its fiber-reinforced nature have shown promising results in animal models in recapitulating the geometrical structure and biomechanical properties of the native meniscus<sup>8,13,14</sup>. Understanding early spatial patterns of cell response within these fiber-reinforced microenvironments remains a goal for optimal design of these scaffolds to replace the meniscus<sup>15</sup>. Fiber-reinforcement for tissue engineering applications has grown substantially in the past decade<sup>16</sup>, with several advances in recapitulating the mechanical properties of load-bearing musculoskeletal tissues, such as the meniscus<sup>8,13,14,17</sup>, tendons<sup>18</sup>, and articular cartilage<sup>19</sup>. Generally, these strategies aim to mimic native aligned tissue by reinforcing a soft biological substrate with a stiffer polymer fiber network, typically composed of synthetic materials such as poly(lactic acid)<sup>20</sup> or poly( $\epsilon$ -caprolactone)<sup>21</sup>. The softer substrate is often utilized for encapsulation of cells within natural materials such as collagen<sup>20,22</sup>, gelatin<sup>23</sup>, and fibrin<sup>24</sup>. Beyond aligned tissues, 3D printed scaffolds have gained popularity recently, especially as customizable, personalized implants<sup>13,25,26</sup>. While the field is moving closer to recapitulating the bulk mechanical properties of native tissues, the balance between biomechanical properties and tissue deposition at the cellular level remains challenging<sup>16</sup>. This is especially important to cell-laden fiber-reinforced gel scaffolds, where neo-tissue eventually bears load as the polymer fiber and substrate network degrades.<sup>8,14,17,27</sup> Many tissue engineering approaches involve fabrication and biomechanical testing of fiber-reinforced scaffolds at the macroscale, yet they rarely consider the microscale cell-biomaterial interactions that likely govern eventual tissue formation. In fact, early dynamics of cell response, in terms of morphological characteristics and marker expression, have been known to mediate eventual tissue deposition and organization in aligned tissues, like the meniscus<sup>28-30</sup>. Furthermore, during development, the properties of the cellular microenvironment in aligned tissues are crucial in driving and maintaining cell phenotype<sup>1,31-35</sup>, and evidence suggests that early cell patterning can mediate extracellular matrix (ECM) architecture<sup>28,36</sup> and ensuing tissue deposition. Therefore, early cell-biomaterial interactions and patterns of cellular

mechanoreponse within these fiber-reinforced microenvironments require a deeper understanding that would aid in optimization of fiber-reinforcement strategies for the repair and replacement of aligned musculoskeletal tissues<sup>26</sup>.

Although morphological and mechano-responsive patterns on 2D matrix microenvironments have been well studied, there remains a knowledge gap in the nuances of 3D matrix mechanosensing<sup>37-39</sup>. Understanding cellular matrix mechanosensing in 3D microenvironments is critical to gaining insight into the factors governing cell behavior *in vivo*, especially in the context of musculoskeletal load-bearing tissues. Towards this, several studies have used ECM-mimetic hydrogel systems, such as fibrin and hyaluronic acid<sup>40-42</sup>. Fibrin, in particular, mimics early wound healing environments that are readily remodeled, exhibits excellent biocompatibility, and is finely tunable<sup>39,43</sup>. Thus, in this study, we utilized fibrin as the soft biological substrate for cells to remodel and respond within a fiber-reinforced gel. Response to and remodeling of the surrounding matrix can be influenced by several factors, leading to variable patterning and differentiation within the microenvironment<sup>28,33,36,44</sup>. Though advances have been made in differentiating cell mechanosensing patterns between 2D and 3D matrix environments, as well as factors involved in 3D sensing such as substrate stiffness and degradability<sup>38</sup>, nuances of cell response in a fiber-reinforced composite scaffold environment remain unclear. Understanding the dynamics by which cells sense within an anisotropic 3D environment can inform design strategies for fiber-reinforced scaffolds at the microscale. Specifically, cells can sense and respond to microenvironmental cues, such as anisotropic structural orientation and depth<sup>45</sup>, biophysical properties of the surrounding matrix (e.g., degradation and mechanics)<sup>27,46</sup>, and proximity to rigid materials (e.g., polymer fiber) in stiff-soft environments<sup>47</sup>. Through mechanosensing of these cues, downstream morphological behavior and patterning of the fiber-reinforced microenvironment can govern eventual tissue deposition and architecture<sup>48,49</sup>. The transcriptional regulator YAP (Yes-associated Protein) serves as a

mediator of matrix mechanosensing<sup>38,50,51</sup>, correlating to dynamics of ECM deposition<sup>38,50-53</sup>.

Therefore, by measuring early YAP nuclear localization and cell morphological features, we can reveal holistic patterns of cell response in stiff-soft fiber-reinforced microenvironments. To our knowledge, early patterns of cell morphological and mechanosensing parameters have not been decoupled in the context of fiber-reinforced microenvironments, highlighting a need to understand the factors involved in cell sensing to optimize fabrication of fiber-reinforced tissue engineering approaches for optimal meniscus replacement.

In addition to the limited consideration of cell sensing and cell-biomaterial interactions within tissue-engineered environments for meniscus replacement, the matrix heterogeneity of the native meniscus is often overlooked. The meniscus is composed of a widely heterogeneous population of cells which can be organized into four major morphologically distinct groups<sup>54</sup>. Two of these groups represent more fibroblast-like cells found more commonly in the outer meniscus, a third group contains rounded, compact chondrocyte-like cells that predominate the inner hyaline-like region of the tissue, and a final group is composed of fusiform-shaped cells found in the superficial meniscus. Together, these cells are commonly referred to collectively as fibrochondrocytes, and the cell groups within this broad class have been shown to produce and deposit varied ECM, both in terms of biochemical composition as well as geometry and organization<sup>55</sup>. The distribution of meniscal fibrochondrocyte morphology and extracellular matrix organization from the inner meniscus (chondrocyte-like cells, Proteoglycan-dense ECM) to the outer meniscus (fibroblast-like cells, circumferential fibrous collagen ECM) is uniquely suited to withstand the dynamic loads experienced by the tissue within the knee joint<sup>56,57</sup>. The heterogeneous ECM distribution of the meniscus leads to variation in the micromechanical properties from inner to outer, collectively making up the complex mechanical profile of the tissue<sup>58</sup>. Generally, proteoglycans with sulfated glycosaminoglycan (GAGs) side chains are found mostly within the inner third portion of the meniscus which contribute to the zone's tissue

compressive properties that mimic articular cartilage. The predominant GAG component found in the meniscus is chondroitin sulfate, composed of a chain of alternating N-acetylgalactosamine and glucuronic acid sugars<sup>59,60</sup>. On the other hand, the middle and outer zones of the meniscus are predominantly composed of circumferentially aligned type I collagen bundles<sup>58</sup>, which allow these portions to handle tensile hoop stresses within the joint<sup>5</sup>. Together, these inner, middle, and outer zones of the meniscus possess vastly different ECM profiles both geometrically and biochemically; these nano and micro-scale nuances are critical to the overall macro-scale properties of the tissue in maintain joint stability in a healthy knee. In order to fully recapitulate regional variations, studies have begun to prioritize precise, zone-specific matrix deposition in tissue-engineered meniscus, though this has not been accomplished in a representative three-dimensional environment<sup>61</sup>.

The design and fabrication of fiber-reinforced scaffolds for anisotropic meniscal tissue regeneration require thoughtful consideration; the balance between time-zero mechanical properties and downstream attributes of newly formed tissue must be tuned to adequately replicate native soft tissue. This balance relies on early cell responses and its translation to eventual deposited tissue dynamics. Specifically, within the context of fiber-reinforced scaffolds, factors such as interstrand spacing<sup>26</sup>, scaffold pore size<sup>62</sup>, and cell-ECM interactions<sup>63</sup> instruct cells in the early cell-biomaterial microenvironment. Furthermore, substrate chemistry and biophysical characteristics, and the rate at which they are remodeled, impact cell response, both in terms of cell-cell communication as well as cell-biomaterial interactions<sup>35,64</sup>. Cell-matrix interactions via integrin-based adhesions are critical towards mechano-sensation and cellular behavior<sup>65,66</sup>, pointing to the ability of cells to adhere to the surrounding three-dimensional matrix as a critical influencer of downstream matrix production. The role of these adhesions in meniscal ECM production and deposition remains unexplored. Additionally, once adhered, the ability of the cell to remodel its provisional ECM network is necessary for nascent tissue

deposition and organization<sup>67,68</sup>. Consideration of these cell-ECM interactions mediated by adhesion and remodeling is essential to regenerate functional meniscal tissue; a thorough understanding of the microenvironmental conditions that may influence this balance can provide the field with avenue by which meniscal ECM can be precisely patterned. Through characterization of cell response under these various conditions, design choices at the microenvironmental level can be made to enhance early cell responses that guide deposited tissue architecture that optimally recapitulates the native meniscus<sup>17,61,69</sup>.

The goals of this study are to 1) investigate spatial patterns of cell response in a fiber-reinforced microenvironment for meniscus replacement; 2) utilize a machine-learning based clustering approach to identify spatially responsive sub-groups within a heterogeneous cell population; 3) understand how alterations of this fiber-reinforced microenvironment mediate these patterns of response; 4) elucidate the effects of altering the biomaterial microenvironment on meniscal fibrochondrocyte (MFC) matrix producing capabilities; and 5) understand how tuning adhesion and remodeling may guide precise meniscal matrix deposition for the ultimate goal of a tissue-engineered meniscus replacement capable of fully recapitulating the zonal heterogeneity of the meniscus. Together, these experimental results displayed the applicability of machine learning in revealing patterns in a heterogeneous environment and the importance of spatial orientation, substrate biophysical properties, and matrix remodeling in governing early cell response and matrix deposition for meniscus tissue engineering.

## Materials and Methods

### Cell Preparation, Culture, and Native Meniscus Sectioning

Marrow stromal cells (MSCs) were isolated from a juvenile (1–3 weeks old) bovine stifle joint (Research 87, Boylston MA). Briefly, subchondral trabecular bone blocks were shaken in heparin-containing (0.2% w/v heparin) Dulbecco's modified Eagle's medium (DMEM), and the resulting solution was centrifuged, resuspended in basal medium with 10% fetal bovine serum (FBS; VWR 97068-085; Lot: 274K20), and plated for expansion. Additionally, medial menisci were isolated from the same joints and chopped into small pieces before being digested in collagenase-containing (0.1% w/v collagenase Type IV) DMEM overnight. Meniscal Fibrochondrocytes (MFCs) were resuspended in basal medium. Cells were then frozen in liquid nitrogen, thawed, and expanded as needed. Passage 1 cells that were only expanded once after thawing were used for all experiments. Additionally, to first understand native meniscal cell alignment in a spatial manner, whole rabbit menisci were cryosectioned and stained for COL1 and CellMask.

### Fibrin gel fabrication and mechanical testing

Prior to cell experiments, acellular fibrin gels were fabricated to evaluate mechanical properties. Fibrinogen from bovine plasma (Sigma F8630; 10, 25, or 50 mg/mL final concentration) and thrombin from bovine plasma (Sigma T4648; 5 U/mL final concentration) were mixed with 200 mM calcium chloride ( $\text{CaCl}_2$ ) in phosphate-buffered saline (PBS) to fabricate gels. To do so, a mixture of thrombin/ $\text{CaCl}_2$ /PBS (5  $\mu\text{L}$ ) was first pipetted onto a glass slide. Next, 5  $\mu\text{L}$  of fibrinogen was pipetted directly onto this drop, pipetting several times to mix prior to fibrinogenesis. Gels were incubated for 1 hour at 37 °C and 5%  $\text{CO}_2$  and suspended in 1X PBS. Gel mechanics were characterized via nano-indentation (Optics 11 Pavone) with a 27

$\mu\text{m}$ -radius spherical probe (0.020 N/m). At least 20 points were tested on each gel, and load-indentation curves were fit with a Hertzian model to obtain an effective Young's modulus.

#### Cell encapsulation and hydrogel culture – Fibrin Gels

To encapsulate MSCs within fibrin gels, passage 1 MSCs were thawed and expanded in basal medium for 5-7 days, until ~75% confluent in 100 mm cell culture dishes. Cells were then trypsinized and added into the thrombin/ $\text{CaCl}_2$ /PBS solution, reaching a final concentration of 1.25 million cells/mL (12,500 cells per 10  $\mu\text{L}$  gel). Gels composed of varying concentrations of fibrinogen (10, 25, or 50 mg/mL) were prepared in an 8-well chambered glass slide (**Fig. 1A**), followed by addition of a 5-0 MonoQ fiber (polyglycolide-co-caprolactone; [PGCL]; ~100  $\mu\text{m}$  diameter; Ethicon) directly into each droplet prior to gelation (1 hour, 37 °C, 5%  $\text{CO}_2$ ). The fiber was placed at the top of the gel to ensure that analyzed cells (near fiber) were not responding to the stiff surface of the glass slide. Following incubation, gels were cultured in chemically defined medium (DMEM, 1% v/v penicillin-streptomycin-fungizone [PSF], 50  $\mu\text{g}/\text{mL}$  vitamin C, 0.1 mM dexamethasone, 40  $\mu\text{g}/\text{mL}$  L-proline, 100  $\mu\text{g}/\text{mL}$  sodium pyruvate, 0.1% v/v ITS liquid medium supplement, 1.25 mg/mL bovine serum albumin [BSA], 5.3  $\mu\text{g}/\text{mL}$  linoleic acid [LA]) supplemented with 10 ng/mL TGF- $\beta$ 3 and low or high concentrations of aprotinin (10 or 100 KIU/mL). Aprotinin inhibits fibrinolysis by preventing plasmin from inducing degradation of crosslinked fibrin. Samples were cultured for three days (37 °C, 5%  $\text{CO}_2$ ), and medium was replaced after 2 days in culture.

#### Immunofluorescent Staining – Fibrin Gels

Following culture, gels were rinsed in PBS and fixed in 10% Carson's buffered formalin for one hour at room temperature (RT). Next, gels were rinsed thrice in PBS and permeabilized (1% Triton X-100 in PBS) for 45 minutes. After three PBS rinses, gels were blocked (3% BSA in

PBS) for 30 minutes. Next, gels were stained for YAP1 (Invitrogen PA5-87568; rabbit polyclonal; 1:200 in 1% BSA) for 60 minutes at RT. Following three PBS rinses, gels were stained with secondary antibody (AlexaFluor 647, goat anti-rabbit; 1:200) and Phalloidin (AlexaFluor 555, 1:400) in 1% BSA for 60 minutes at RT. Gels were rinsed again and nuclei were stained with DAPI (1:1000 in 1% BSA) for 20 minutes at room temperature. Chambers were removed, and samples were mounted with Prolong Gold and a rectangular coverslip (24 mm x 50 mm) was placed on top.

### Imaging and Cell Parameter Extraction – Fibrin Gels

A Nikon A1R confocal microscope was used to visualize cells in fiber-reinforced gels (Lens specifications: Nikon MRD00205, 20X, numerical aperture 0.75). Cells within 300  $\mu\text{m}$  of the fiber (perpendicular to the fiber surface) and within the top 100  $\mu\text{m}$  of the fiber height were used for analysis in order to only include cells responding to the fiber and not to the glass slide surface. ND2 images were first processed in ImageJ FIJI to obtain maximum intensity z-stack projections and split channels (DAPI, phalloidin, YAP) into individual TIFF files. Next, a custom CellProfiler<sup>70</sup> pipeline was created to identify individual nuclei (from the DAPI channel), their encompassing cells (from the phalloidin channel), and single-cell YAP intensities in the nucleus, cytoplasm, and perinuclear ring using the YAP channel. From these images, 23 measurements were acquired for each identified cell ( $n = 943$  cells). Cell and nuclear shape measurements included: Area, Compactness, Eccentricity, Form Factor ( $4 \frac{\pi \cdot \text{Area}}{\text{Perimeter}^2}$ ), Major Axis Length, Max Feret Diameter, Minor Axis Length, Perimeter, Solidity, Angle Deviation, and Aspect Ratio. YAP parameters measured were nuclear/cytoplasmic intensity ratio and nuclear/perinuclear intensity ratio. In addition, distance from each cell nuclear centroid to its closest point on the polymer fiber were acquired for each measured cell. From these raw cell

features, conformity index (Eq.1) and morpho-mechanoresponse (Eq.2) parameters were calculated for each cell. Conformity index describes the degree to which individual cells align to the morphology of the stiff polymer fiber, considering both cell spreading and cell angle to output a value between 0 (less conforming) and 1 (more conforming). Morpho-mechanoresponse considers both conformity index and YAP nuclear/cytoplasmic intensity ratio to output a singular value describing the degree to which individual cells sense and conform to the stiff polymer fiber.

$$\text{Conformity Index} = |\cos(\text{Angle Deviation})| * \left(1 - \frac{1}{\text{Aspect Ratio}}\right) \quad (\text{Eq.1})$$

$$\text{Morpho - mechanoresponse} = \text{Conformity} * \frac{\text{YAP}_{\text{Nuc}}}{\text{YAP}_{\text{Cyto}}} \quad (\text{Eq.2})$$

### Analysis Pipeline, PCA, and AHC – Fibrin Gels

After acquisition of 23 parameters for 943 cells in one of six fiber-reinforced gel groups (25, 50, or 100 mg/mL fibrinogen in medium supplemented with 10 or 100 KIU/mL aprotinin), data were standardized by subtracting the mean from each value and dividing by standard deviation. Next, PCA using a correlation matrix was run on this set of 943 cells using XLSTAT software (Addinsoft Corporation), outputting five principal components (PCs; **Fig. 1B**), comprising 83.78% of the variability present in the total data set (80% variability was used as a threshold). Weighted factor scores for each PC were outputted for each individual cell. Next, the five PC scores for each cell were used for Agglomerative Hierarchical Clustering (AHC) analysis in XLSTAT. Clusters were determined using dissimilarity (Euclidian Distance), and Ward's method was used for agglomeration of clusters. Using the Hartigan Index, three was determined as the optimal number of clusters to ensure maximum distance between clusters<sup>71,72</sup>. AHC divided the heterogeneous set of 943 cells into cluster 1 (n = 351), cluster 2 (n = 450), and

cluster 3 (n = 142). These clusters were used to distinguish patterns of cell response in different cell families (**Fig. 1C**).

#### Methacrylated Gelatin/Hyaluronic Acid Gel Fabrication

PhotoHA and PhotoGel lyophilized biomaterial (Advanced Biomatrix) were used to make MeHA and GelMA hydrogels. Gels were fabricated at three different combinations of GelMA/MeHA: 100% GelMA (100G; 5% w/v), 75% GelMA and 25% MeHA (75G25H; 3.75/0.5% w/v), and 50% GelMA and 50% MeHA (50G50H; 2.5/1.0% w/v). To fabricate gels, the proper amount of lyophilized biomaterial was weighed and sterilized for one hour with UV light and dissolved in sterile PBS. 0.1% w/v LAP was used as a photoinitiator and mixed into the gel solution prior to crosslinking. On a sterile glass slide, 80  $\mu$ L of gel solution were added in a single puddle surrounded on both sides by 0.25 mm silicon spacers. A 24 mm x 50 mm glass coverslip was placed over the gel solution puddle and spacers and the solution was exposed to blue light for 5 minutes to allow for adequate crosslinking (**Fig. 2A**).

#### Nascent Matrix Labeling and Culture of GelMA/MeHA Hydrogels

To encapsulate MFCs within GelMA/MeHA gels, passage 1 MFCs were thawed and expanded in basal medium for 5-7 days, until ~75% confluent in 100 mm cell culture dishes. Cells were then trypsinized and added into the GelMA/MeHA/LAP solution, reaching a final concentration of 1 million cells/mL (80,000 cells per 80  $\mu$ L gel). These gels were fabricated without the inclusion of a PGCL fiber, generating a free 3D environment to solely investigate the effects of surrounding biomaterial on cell response. Following crosslinking as detailed previously, the 0.25 mm thick sheet of gel was cut into 1 mm x 1 mm squares which were then

transferred into wells of an 8 chambered slide (**Fig. 2B**). Half of these gels were labeled for nascent protein and half were labeled for nascent GAG (specifically, N-Acetylgalactosamine, a component of chondroitin sulfate, the predominant proteoglycan found in meniscal ECM). To accomplish this metabolic labeling, gel constructs were cultured in either AHA Media consisting of glutamine-, methionine-, and cystine-free high-glucose DMEM,  $0.1 \times 10^{-6}$  M dexamethasone (Sigma-Aldrich),  $4 \times 10^{-3}$  M GlutaMAX supplement (Thermo Fisher),  $0.201 \times 10^{-3}$  M L-cystine (Sigma-Aldrich), 100  $\mu$ g/mL sodium pyruvate (Cellgro), 1.25 mg/mL bovine serum albumin (BSA), 0.1% insulin-transferring-selenium (ITS) + premix, 50  $\mu$ g/mL ascorbate 2-phosphate, 40  $\mu$ g/mL L-proline, and 1% penicillin-streptomycin-amphotericin, further supplemented with 10 ng/mL TGF- $\beta$ 3, and  $0.1 \times 10^{-3}$  M AHA or GalNAz media consisting of glutamine-, methionine-, and cystine-free high-glucose DMEM,  $0.1 \times 10^{-6}$  M dexamethasone,  $4 \times 10^{-3}$  M L-glutamine,  $0.201 \times 10^{-3}$  M L-cystine, 100  $\mu$ g/mL sodium pyruvate, 1.25 mg/mL BSA, 0.1% ITS+ Premix, 50  $\mu$ g/mL ascorbate 2-phosphate, 40  $\mu$ g/mL L-proline, and 1% penicillin-streptomycin-amphotericin, further supplemented with 10 ng/mL TGF $\beta$ -3 and  $0.05 \times 10^{-3}$  M GalNAz<sup>73,74</sup>. Samples were cultured for 3, 7, or 14 days (37 °C, 5% CO<sub>2</sub>), and metabolic labeling media was replaced each day from days 1-7 and every other day following day 7.

#### Immunofluorescent Staining – GelMA/MeHA Gels

Following culture, gels were rinsed 1X in PBS and blocked (3% BSA in PBS) for 30 minutes at 37 °C and 5% CO<sub>2</sub>. Next, gels were stained with 3 mM DBCO-555 solution (Vector Laboratories) in 1% BSA in PBS for 40 minutes at 37 °C and 5% CO<sub>2</sub>. After 3X PBS rinse, gels were fixed in 10% Carson's buffered formalin for one hour at room temperature (RT). Next, gels were rinsed 3X in PBS and stained for CellMask Deep Red (647) plasma membrane stain (Invitrogen; 1:1000 in 1% BSA). Gels were rinsed again and nuclei were stained with DAPI

(1:1000 in 1% BSA) for 20 minutes at room temperature. Chambers were removed, and samples were mounted with Prolong Gold and a rectangular coverslip (24 mm x 50 mm) was placed on top.

#### Imaging and Cell Parameter Extraction – GelMA/MeHA Gels

A Nikon A1R confocal microscope was used to visualize cells in GelMA/MeHA gels (Lens specifications: Nikon MRD00205, 20X, numerical aperture 0.75). ND2 images were first processed in ImageJ FIJI to obtain maximum intensity z-stack projections and split channels (DAPI, DBCO, CellMask) into individual TIFF files. Next, a custom CellProfiler70 pipeline was created to identify individual nuclei (from the DAPI channel), their encompassing cells (from the CellMask channel), and the surrounding ECM (either protein or GAG) of each cell stained with DBCO. From these images, 23 measurements were acquired for each identified cell. Cell and nuclear shape measurements included: Area, Compactness, Eccentricity, Form Factor ( $4 * \text{Area} / \text{Perimeter}^2$ ), Major Axis Length, Max Feret Diameter, Minor Axis Length, Perimeter, Solidity, Angle Deviation, and Aspect Ratio. Additionally, integrated intensity of the ECM ring surrounding each cell was quantified as a metric of matrix deposition.

#### Pentanoate-Functionalized Hyaluronic Acid Synthesis and Peptide Functionalization

Pentanoate-Functionalized Hyaluronic Acid (PHA) Hydrogels were fabricated from a precursor solution (2% w/v in PBS, 30% reactive -ene functionalized) containing 0.1% w/v LAP (photoinitiator), and total crosslinker concentration inclusive of all options maintained at 1:1 molar ratio of thiol:ene on the PHA. The integrin binding RGDS sequence was incorporated with a cysteine terminated peptide sequence (10 amino acid dithiol, KCGRGDSGCK, Genscript) for

thiolene click chemistry into the hydrogels. A scrambled sequence (10 amino acid scrambled dithiol, KCGRDGSGCK) was used as a negative control. MMP2 cleavable sequence (GCRDGPQGIWGQDRCG) was included for cell-based remodeling, with a scrambled sequence (GCRDGDQGIAGFDRCG) as negative control. Figure 3A illustrates the hydrogel synthesis route and study design to evaluate the interplay between adhesion and remodelability. For each hydrogel formulation detailed in Figure 3B, poly(ethylene glycol) (PEG) dithiol (1k, Creative PEGWorks) was included at 0.5:1 thiol:ene molar ratio to maintain controlled crosslink density and thus compressive properties across all hydrogel systems. The other half of crosslinkers was composed of iterations of adhesive and remodel-able peptides (no, low, high) to modulate cell behavior as detailed in Figure 3B. PHA gels were fabricated similarly to GelMA/MeHA gels detailed above and cultured in metabolic labeling media to stain for nascent matrix. Additionally, an identical pipeline of culture, staining, imaging, and cell data acquisition were used for PHA hydrogels as were used for GelMA/MeHA constructs.

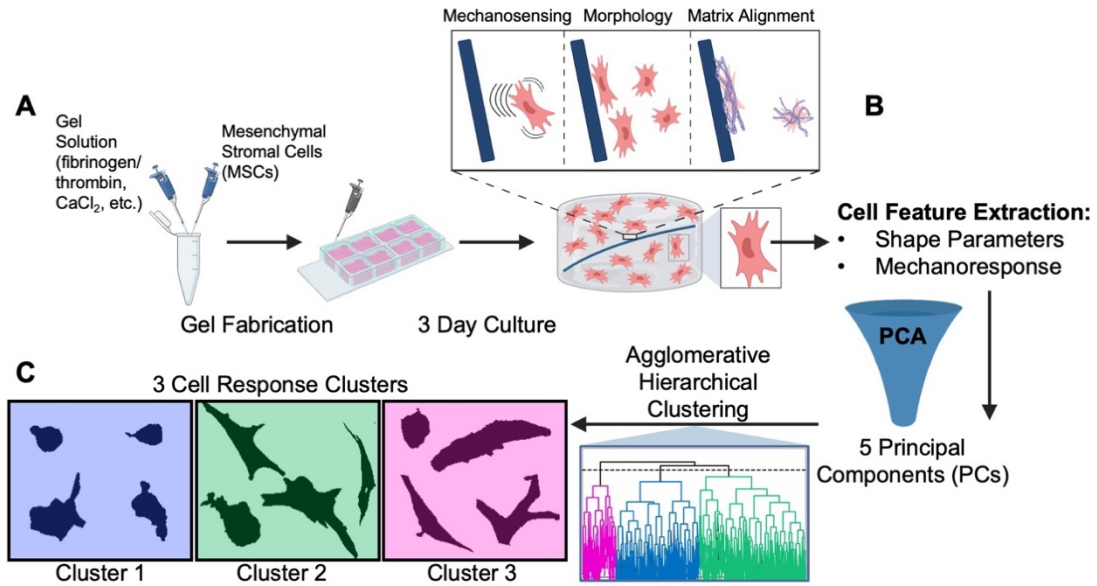


**Figure 1. Cell Feature Acquisition in Fiber-Reinforced Microenvironment.** [A] Simulation of fiber-reinforced microenvironment via fibrin gel fabrication and culture. [B] Cell feature extraction ( $n=23$ ) and Principal Component Analysis (PCA) to project onto 5 Principal Components (PCs). [C] Clustering of total cells ( $n=943$ ) into three distinct clusters based on level of response.

(Created with BioRender.com)

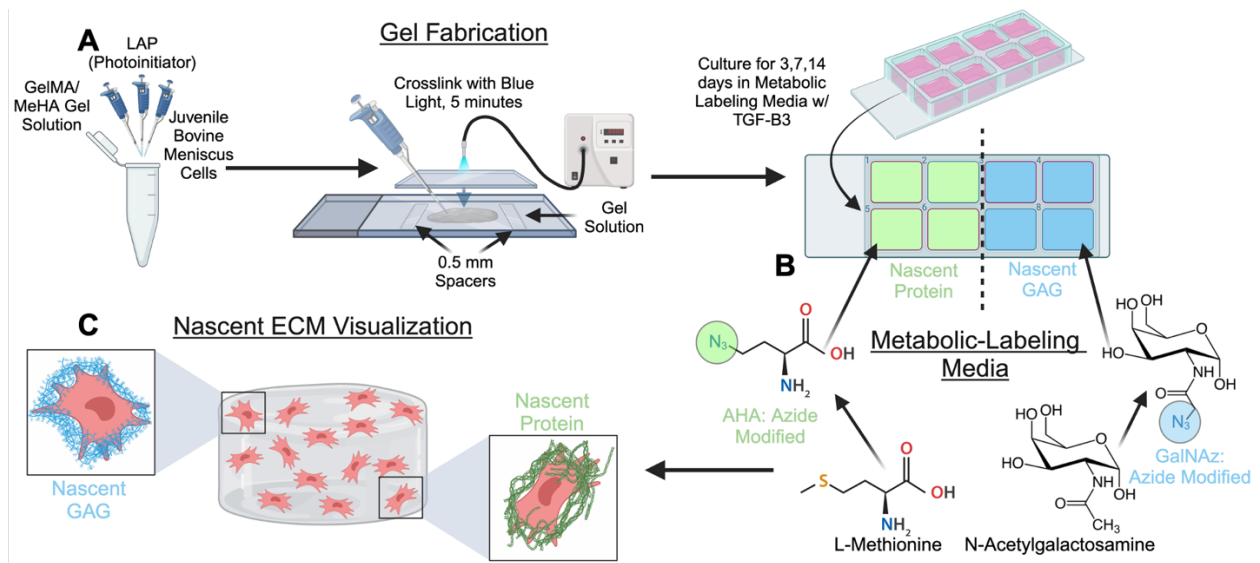


**Figure 2. Nascent Matrix Labeling of Meniscal Fibrochondrocytes.** [A] Fabrication of GelMA/MeHA hydrogels containing encapsulated juvenile bovine MFCS. [B] Metabolic-Labeling of nascent protein and nascent GAG through replacement of L-Methionine with L-Azidohomoalanine (AHA) and N-Acetylgalactosamine with N-azidoacetylgalactosamine in media. [C] Visualization of nascent protein and nascent GAG in 3D hydrogels following culture.

(Created with BioRender.com)

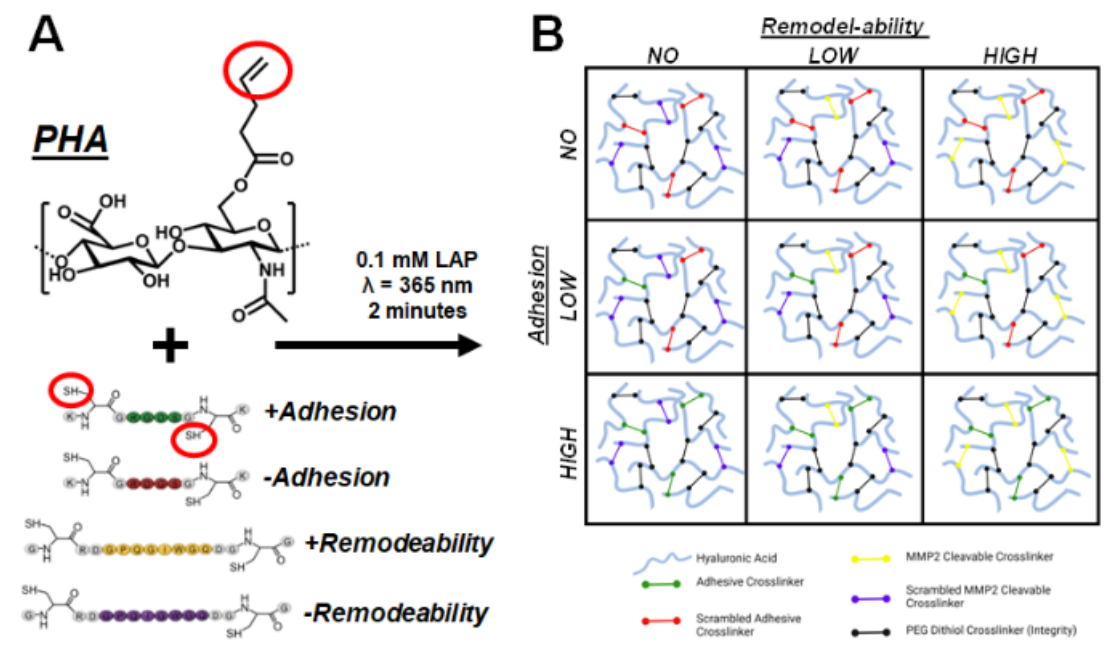


**Figure 3. Pentanoate-Functionalized HA MMP-Cleavable and RGD Peptide**

**Functionalization.** The inclusion of adhesive (RGDS) and remodel-able (MMP2 cleavable) crosslinkers, and their scrambled counterparts, enables precise tuning of adhesion and remodel- ability. [A] Pentenoate functionalized hyaluronic acid (PHA) crosslinking reaction. [B] Study permutations to achieve hydrogels permutations with no, low, and high adhesion and remodel-ability.

### Statistics

Linear regression analysis was used to analyze scatterplot data. For column graphs, outliers were identified using the ROUT method, and normality was tested with the D'Agostino & Pearson test. Next, the Kruskal-Wallis non-parametric ANOVA test (distributions were found to be non-normal) was used to compare groups with 2 or more comparisons, using Dunn's multiple comparisons test to determine significance between groups. The Mann-Whitney non-parametric t-test was utilized for comparisons between two groups. In all violin plots, distribution of

individual data points is shown, the bold middle line in each plot indicating median, and two dotted lines above and below indicating quartiles. In each graph, \*, \*\*, \*\*\*, and \*\*\*\* represent  $p < 0.05$ ,  $0.01$ ,  $0.001$ , and  $0.0001$ , respectively.

## Results

### Relationships between cell features and fiber distance within stiff-soft microenvironments are highly heterogeneous

Following 3-days of MSC culture within fiber-reinforced microenvironments, spatial heterogeneity was present in terms of single-cell conformity and mechanoresponsiveness. Considering several cell shape parameters such as angle deviation from fiber, aspect ratio, and conformity, considerable variability was seen on a cell-to-cell basis (**Fig. 4A**). Both conformity and YAP nuclear localization values for cells within the entire population ( $n = 943$ ) exhibited a statistically significant negative correlation ( $p = 0.0017$ ,  $p < 0.0001$ , respectively) with distance from the fiber (**Fig. 4B & 4C**). Consequently, morpho-mechanoresponse values for this set of cells also exhibited a negative correlation (**Fig. 4D**;  $p < 0.0001$ ). However, all three of these correlations were weak ( $R^2 < 0.1$ ) despite a statistically significant deviation from a slope of 0, motivating the need for machine learning-based higher-order strategies to parse through heterogeneity within the data set.

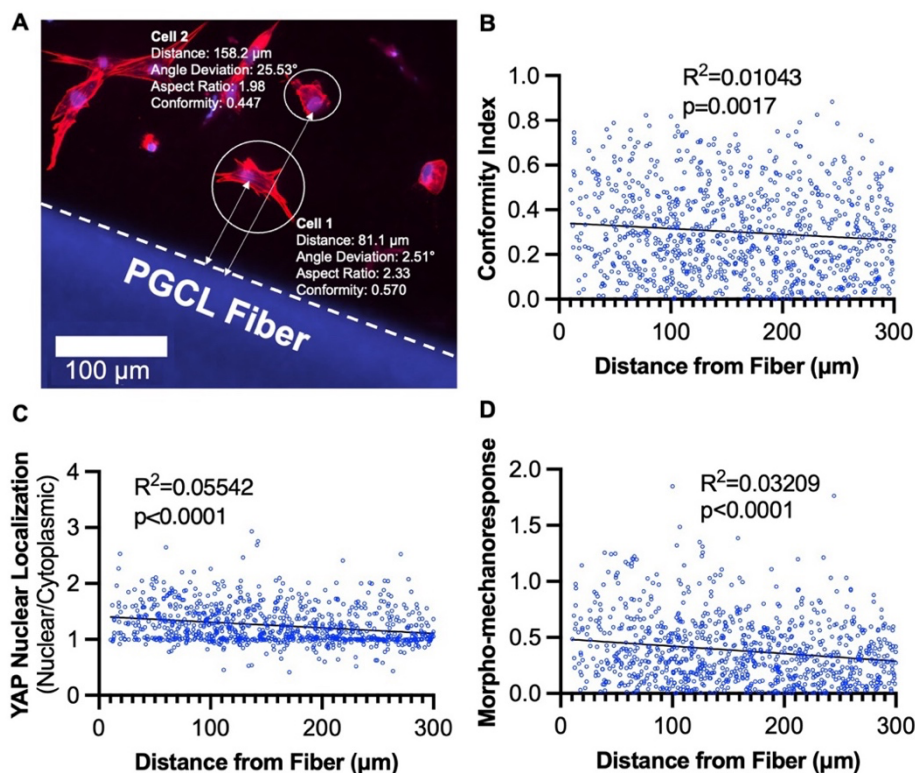


**Figure 4. Cell shape and nuclear response to a stiff polymeric fiber in a fiber-reinforced environment is highly heterogeneous.** [A] Distance, angle deviation, and YAP Nuclear/Cytoplasmic Ratio measurements of individual cells around a polymer fiber. [B] Conformity index, [C] YAP Nuclear Localization, and [D] Morpho-mechanoreponse values of cells ( $n=943$ ) within a 300  $\mu\text{m}$  area around a fiber as a function of distance from the fiber.

### 3D cell mechanoreponse decreases in a stiffness-dependent manner

To investigate the influence of gel substrate mechanics on patterns of cell behavior in the fiber-reinforced microenvironment, MSCs in stiff-soft environments comprised of varying fibrinogen concentrations (50, 25, or 10 mg/mL) and low aprotinin (10 KIU/mL) were evaluated. As expected, lower fibrinogen concentration resulted in lower gel stiffness (**Fig. 5A**). MSCs in lower stiffness (10 mg/mL fibrinogen) gels also exhibited greater morphological and nuclear

response, with slightly higher conformity index values and significantly higher YAP nuclear localization (Fig. 5B & 5C). Overall, morpho-mechanoresponse was significantly greater for cells encapsulated in 10 mg/mL fibrinogen fibrin gels (Fig. 5D), indicating the importance of substrate mechanics in a cell's ability to respond to biophysical stimuli at the cell-fiber interface.

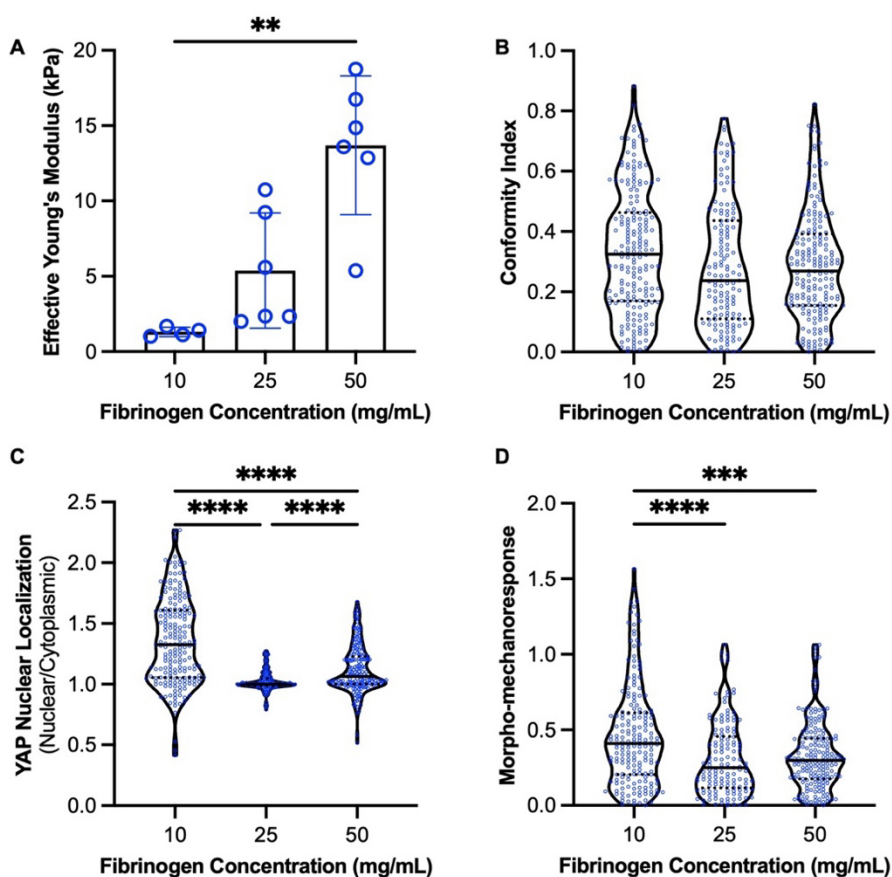


**Figure 5. Cell response to polymeric fiber is heightened in lower-stiffness (lower fibrinogen content) fibrin constructs.** [A] Effective Young's modulus of gels fabricated with varying fibrinogen concentrations. [B] Conformity index of cells in varying Fibrinogen Concentration fibrin gels (all low aprotinin) [C] YAP nuclear localization ratio of cells in varying Fibrinogen Concentration fibrin gels (all low aprotinin) [D] Morpho-Mechanoresponse of cells in varying Fibrinogen Concentration fibrin gels (all low aprotinin) \*\*, \*\*\*, \*\*\*\* represent  $p < 0.01$ , 0.001, 0.0001, respectively.

PCA-AHC analysis is able to separate heterogeneous MSC populations into three sub-groups

Due to the high heterogeneity observed in the holistic analysis of our large MSC population, we employed a PCA-AHC clustering approach to separate the cells into distinct sub-groups. We first projected 23 input variables calculated for each cell to 5 principal components (PCs) which comprised 83.78% of the cumulative variability in the data set (**Fig. S1**). These input variables each contributed differentially to each PC (**Fig. 6A**), with each PC correlating to each parameter to varying extents (**Fig. 6B**). PC1, responsible for 37.54% of the variability, was relatively evenly contributed by all parameters (largest contributor: major axis length, 8.17%), with cell and nuclear length parameters (axis length, perimeter, area) contributing most significantly. PC2, responsible for 20.60% of the variability, similarly correlated to greater cell length parameters, but correlated negatively to nuclear length parameters. Interestingly, PC4 (7.15% variability) was strongly linked to YAP parameters (~40% contribution each), and PC5 (6.31% variability) was strongly linked to cell and nuclear angle deviation (~46% each). Together, these PCs were used for agglomerative hierarchical clustering into three distinct clusters, shown by a PC1 versus PC2 plot in **Fig. 6C**. These three clusters also demonstrated mild separation when PC1 was plotted versus distance from fiber (**Fig. 6D**).

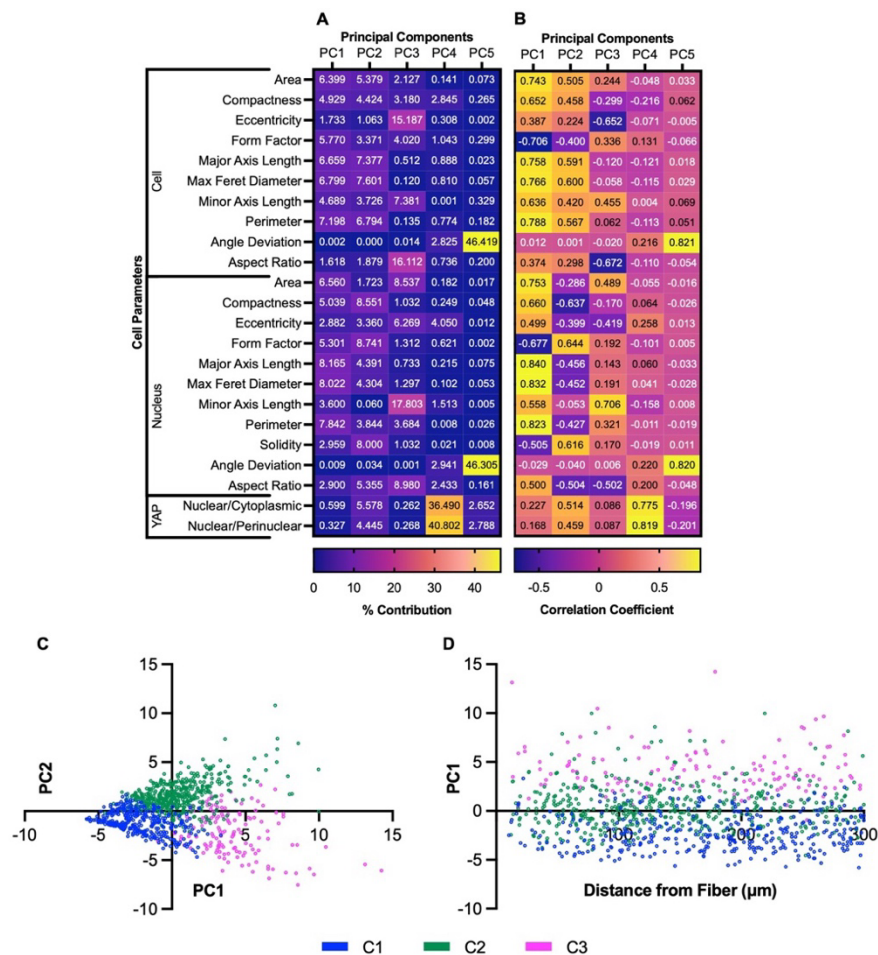


**Figure 6. A heterogeneous set of cells within a simulated fiber-reinforced hydrogel microenvironment can be clustered using Principal Component Analysis followed by Agglomerative Hierarchical Clustering.** [A] Contributions of each cell parameter to each principal component by percentage. [B] Correlations between each cell parameter and principal component. [C] Separate Cell clusters depicted on a PC2 vs. PC1 factor score plot. [D] PC1 factor score of cells from 0-300 μm from fiber, colored by cluster.

#### PCA-AHC analysis reveals MSC clusters with distinct cellular features

The three clusters identified from the PCA-AHC analysis were compared with regards to morphological and mechanoresponse metrics. Cluster 2 cells displayed the highest conformity index measurements, followed by cluster 3, then cluster 1 (**Fig. 7A**). Cluster 2 cells also

displayed the highest levels of YAP nuclear localization ( $p < 0.0001$ ), and cluster 1 cells exhibited the lowest levels centered around a YAP nuclear ratio of 1. Cluster 3 cells exhibited a YAP response between clusters 1 and 2 (**Fig. 7B**). Considering both morphological and mechanosensing responses, cluster 2 cells exhibited the greatest morpho-mechanoreponse followed by cluster 3 cells and cluster 1 cells, with all groups demonstrating statistically significant differences from one another (**Fig. 7C**). A cumulative distribution plot of morpho-mechanoreponse measurements further highlights this separation between clusters (**Fig. 7D**). Based on these findings, the clusters were renamed by increasing morpho-mechanoreponse (Cluster 1 labeled LR for Low Response; Cluster 2 labeled HR for High Response; Cluster 3 labeled MR for Medium Response) for subsequent spatial analyses.

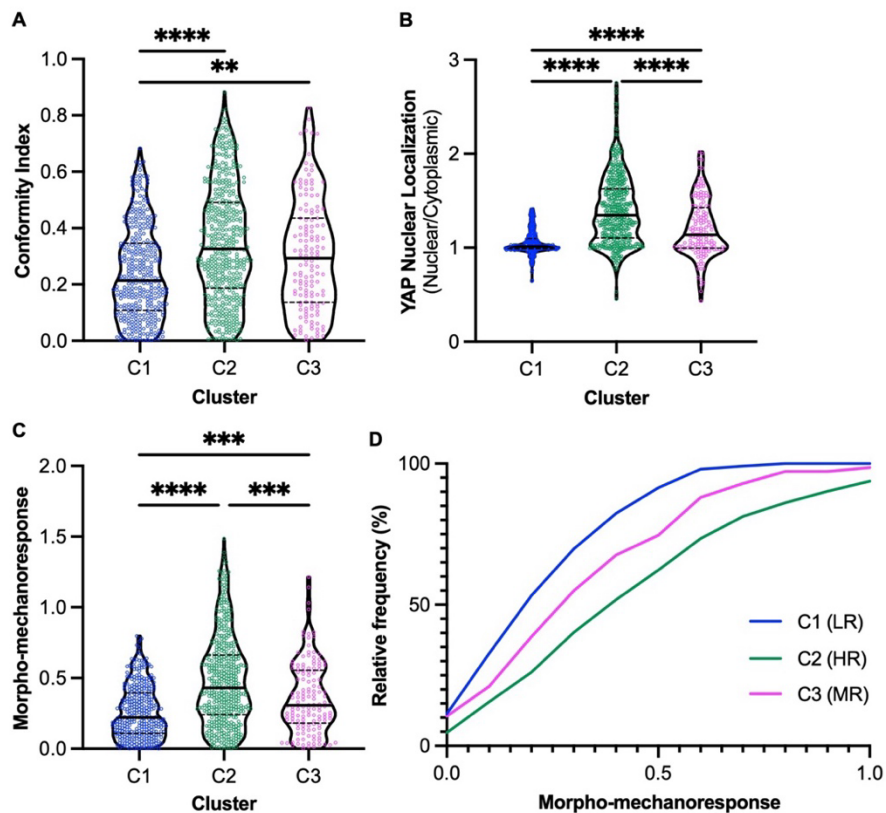


**Figure 7. Classification of acquired cell clusters based on cytoskeleton and nuclear response parameters. HR=High Response, MR=Medium Response, LR=Low Response.**

[A] Conformity index of cells in each cluster (0-1) [B] YAP nuclear localization of cells in each cluster [C] Morpho-mechanoresponse of cells in each cluster. [D] Cumulative Distribution plot depicting the Morpho-mechanoresponse of cells in each cluster. Clusters assigned as: C1 = Low Response (LR), C2 = High Response (HR), C3 =Medium Response (MR). \*\*, \*\*\*, \*\*\*\* represent  $p < 0.01$ , 0.001, 0.0001, respectively.

#### Cells localized to rigid fibers in stiff-soft microenvironments according to cluster responsiveness

After clustering the heterogeneous MSC data set into HR, MR, and LR groups, spatial patterning of these cell families around the fiber was examined. MSCs in the HR cluster appeared to localize closer to the fiber, while cells in the LR group seemed to localize further, suggesting a distance-dependent trend of response (**Fig. 8A**). Upon quantification, HR cells were located significantly closer to the fiber compared to MR and LR cells (**Fig. 8B**). In terms of distribution of cells in each cluster, the frequency distribution of HR cells was right skewed (skewness = 0.39), while the distributions of MR and LR cells were left skewed (skewness = -0.25, -0.24, respectively; **Fig. S2**), further illustrating the distance-dependent patterning of the microenvironment. Furthermore, when separating the 300  $\mu\text{m}$  region of interest into four 75  $\mu\text{m}$  bins, the proportion of HR cells showed a clear decrease from the first to fourth bin. In contrast, LR cells showed the opposite trend (increase from first to fourth bin), while MR cells seemed to be scattered evenly throughout the stiff-soft microenvironment (**Fig. 6C**).

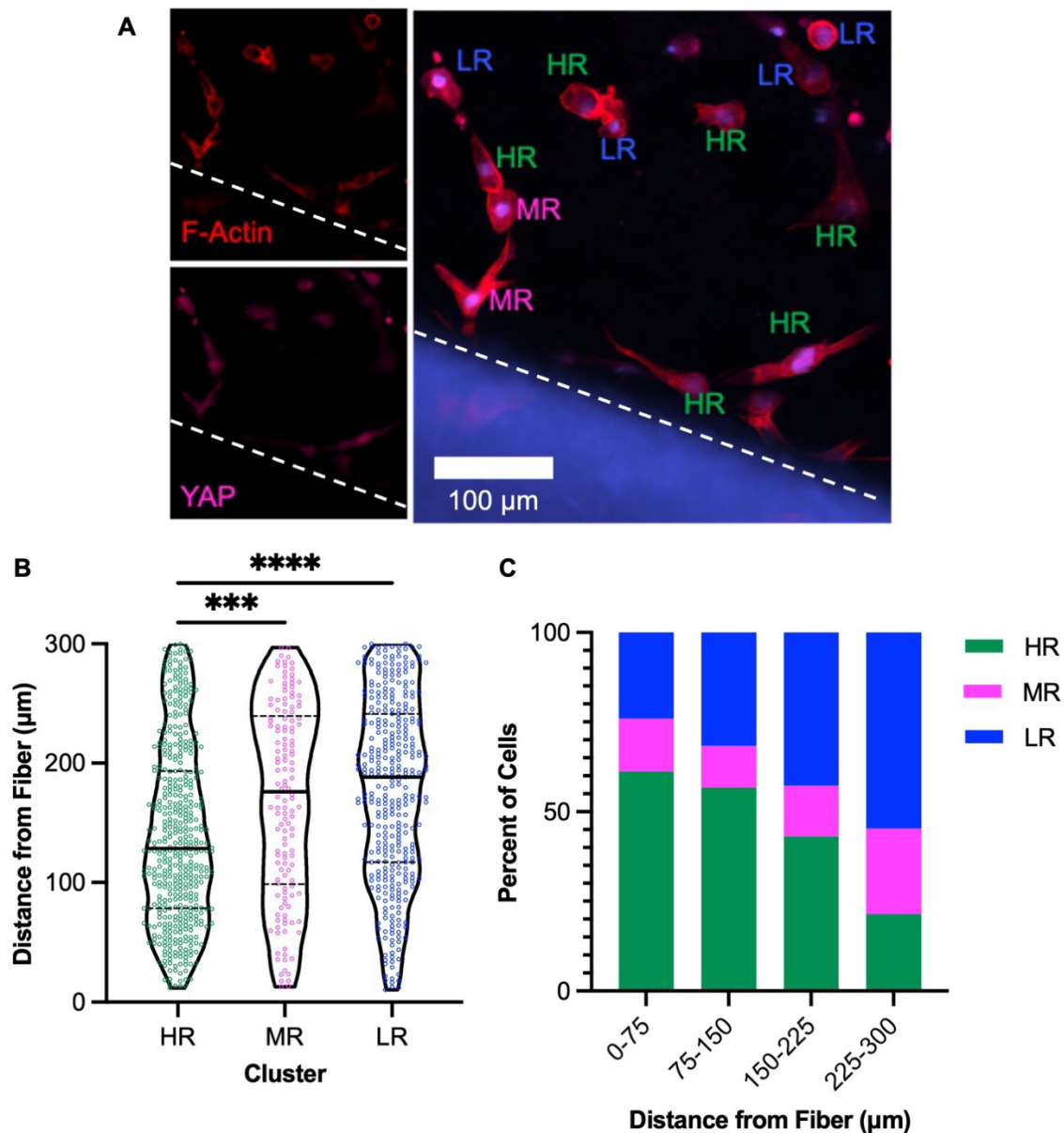


**Figure 8. Cell clusters localize differentially in fiber-reinforced micro-environment.** [A] Cells proximal to fiber labeled by cluster. HR=High Response, MR=Medium Response, LR=Low Response [B] Distances of all cells ( $n=943$ ) from each cluster from the fiber. [C] Percentages of each cell cluster (All Cells) within different regions around fiber. \*, \*\*\*, \*\*\*\* represent  $p < 0.05$ , 0.001, 0.0001, respectively.

### Stiffness and matrix remodeling in fiber-reinforced microenvironment

After establishing that the MSCs in the HR, MR, and LR clusters localized to prescribed distances from the fiber in stiff-soft microenvironments, we next sought to use the identified clusters to better investigate the impacts of gel stiffness (controlled by fibrinogen concentration) and gel remodeling (modulated by aprotinin dosage) on cell responses. In HR cells specifically, morpho-mechanoresponse of cells significantly increased in softer (lower fibrinogen concentration) gel environments (**Fig. 9A**). However, no significant differences were seen in terms of location of HR cells, relative to the fiber, in different stiffness environments (**Fig. 9B**). Similar trends, albeit not as statistically significant, were seen in MR and LR cells (**Figs. S3A, S3B**). Interestingly, higher aprotinin dosage over three days had no significant effect ( $p = 0.7081$ ) on morpho-mechanoresponses of HR cells (**Fig. 9C**) but led to significantly ( $p = 0.0005$ ) closer localization to the fiber (**Fig. 9D**). Again, similar trends were seen in other clusters in terms of morpho-mechanoresponse, but not distance (**Figs. S4A, S4B**).

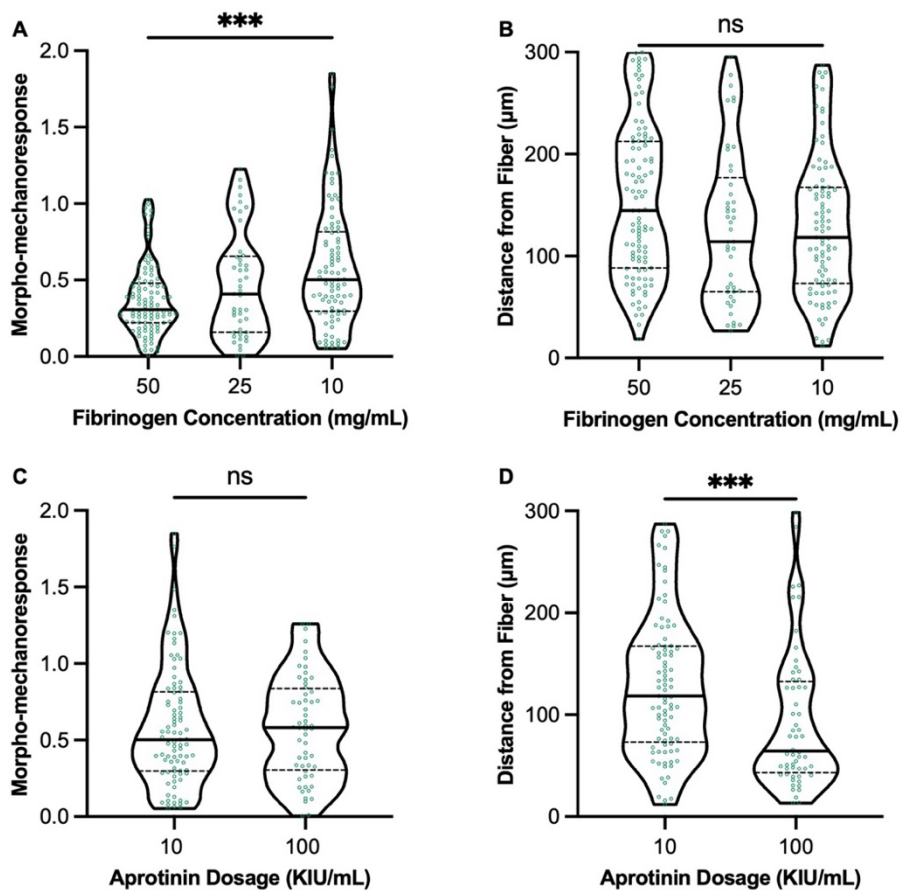


**Figure 9. Stiffness of hydrogel substrate and fibrin remodeling capacity differentially influence level of morpho-mechanoresponse and spatial response of highly responsive cells in fiber-reinforced microenvironment.** [A] Morpho-mechanoresponse and [B] Distance from fiber of HR cells in fibrin gels of varying fibrinogen concentration. [C] Morpho-mechanoresponse and [D] Distance from fiber of HR cells in fibrin gels supplemented with 10 and 100 KIU/ml concentrations of aprotinin. \*\*\* represents  $p < 0.001$ .

### Zonal Heterogeneity of the Native Meniscus

Within the native rabbit meniscus, circumferentially oriented and aligned collagen-rich matrix was observed by COL1 staining. Aligned collagen fibers were observed throughout the full meniscus, from inner to outer (**Fig. 10A**). However, heterogeneity was observed on the cell-scale, with nuclear aspect ratio (NAR) lowest in the inner zone ( $p < 0.0001$ ) and highest in the outer zone ( $p < 0.0001$ ), indicating an increase level of elongated cells from inner to outer meniscus (**Fig. 10B**). Additionally, multicellular aligned strings of 6-12 cells were observed throughout the meniscus, but were particularly predominant in the outer third of the tissue. (**Fig. 10C**)

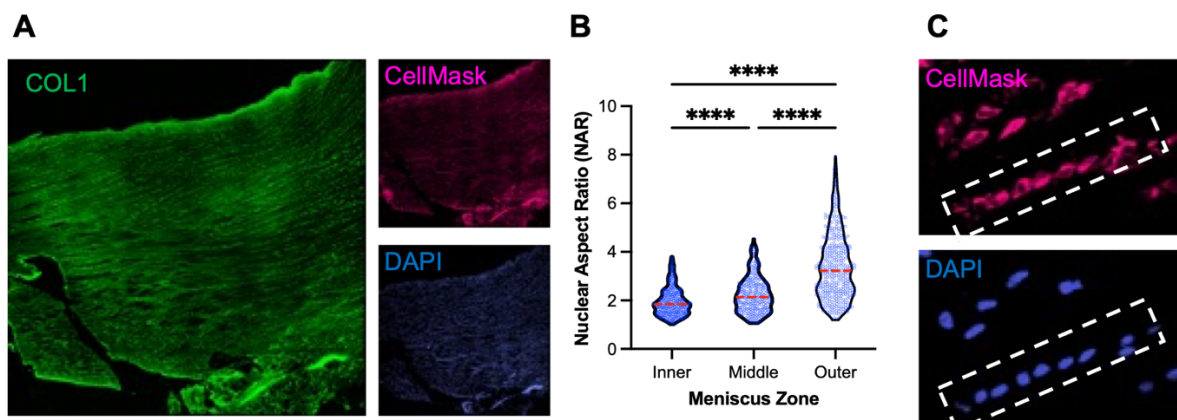


**Figure 10. Meniscus Anisotropy.** [A] Type I collagen (Col1), CellMask (membrane) and DAPI (nucleus) of rabbit meniscus, showing alignment in both inner and outer zones. [B] Nuclear Aspect Ratio (NAR) of cells in each meniscus zone. [C] Identification of multicellular meniscal clusters found throughout the rabbit meniscus.  $n > 300$  cells per zone \*\*\*\* represents  $p < 0.0001$

### Nascent Matrix Alignment Plasticity

Within MFC hydrogel constructs (100G) metabolically labeled to visualize nascent protein, a progression in nascent matrix alignment from 3 to 14 days was readily observed (**Fig. 11A**). At 3 days, small multicellular clusters were observed with minimal nascent matrix deposited around each cell and interspersed between cells within clusters. By 7 days, alignment of these multicellular clusters became more apparent with significant nascent matrix deposition and a clear anisotropy demonstrated by the cluster. Finally, by 14 days a robust sheet of nascent matrix could be clearly observed, with elongated nuclei interspersed within highly aligned, organized matrix. Additionally, incorporation of MeHA within GelMA hydrogels seemed to reduce the level of anisotropy observed throughout the nascent matrix deposited after 14 days (**Fig. 11B-D**), with the 50G50H gel construct yielding a randomly oriented, unorganized ECM. Quantifying goodness of fit of nascent ECM to the preferred orientation determined by fitting with a Gaussian function on 50  $\mu\text{m}$  x 50  $\mu\text{m}$  sections of each gel, it was observed that high incorporation of MeHA in the 50G50H group significantly reduced anisotropy of nascent matrix compared to 100G and 75G25H groups ( $p < 0.0001$ ), though there was no significant difference between the 100G and 75G25H groups themselves ( $p = 0.5811$ ) (**Fig. 11E**).

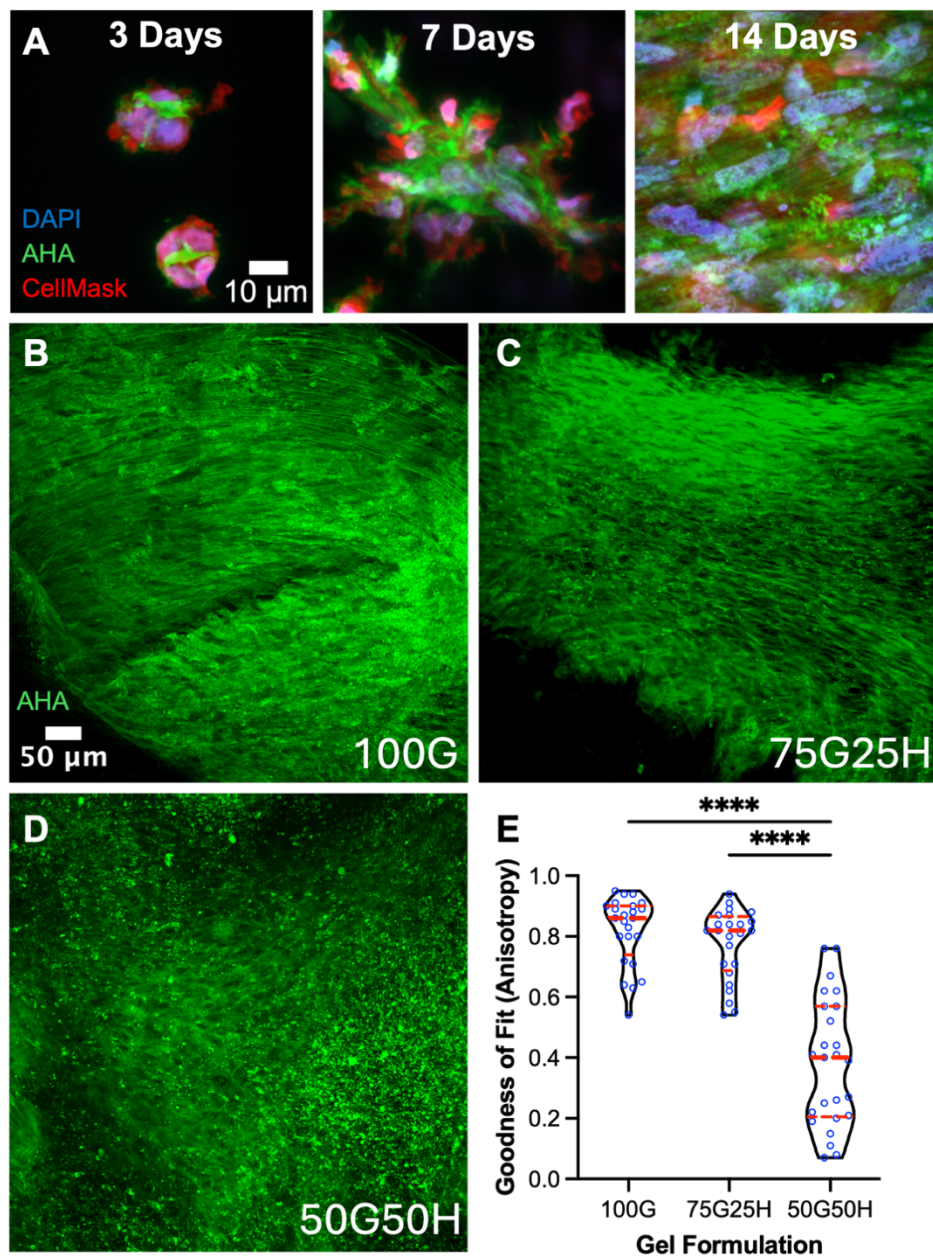


**Figure 11. MFC Matrix Alignment Progression and Plasticity.** [A] Organization and maturation of meniscal cell ECM from 3-14 days in BC 100% GelMA hydrogel environment [B] 2- week representative image of nascent protein organization in 100G hydrogel, followed by [C] 75G25H, and [D] 50G50H [E] Goodness of fit of deposited aligned matrix measured on 50  $\mu$ m x 50  $\mu$ m sections of each environment. n = 25 points per group \*\*\*\* represents  $p < 0.0001$ .

### Precise Matrix Deposition by Mensical Fibrochondrocytes

At an earlier 3-day timepoint, the surrounding biomaterial microenvironment seemed to influence the amount as well as the composition of deposited nascent matrix. Incorporation of MeHA within GelMA hydrogels seemed to inhibit nascent protein deposition around and within multicellular clusters compared to the 100G gel formulation (**Fig. 12A**). Through quantification of integrated intensity of nascent protein found in the ECM ring around each cell, a clear drop-off in nascent protein deposition was seen with the addition of MeHA into the GelMA microenvironment (**Fig. 12B**). Nascent Protein (NP) deposition around MFCs was significantly higher in the 100G formulation compared to the 75G25H and 50G50H constructs ( $p < 0.0001$ ) while there was no significant difference in NP integrated intensity between the 75G25H and 50G50H groups ( $p = 0.3708$ ). On the other hand, an opposite effect was seen with nascent N-Acetylgalactosamine (Gal) after incorporation of MeHA. It was observed that incorporation of MeHA and into GelMA hydrogels seemed to increase deposition of nascent Gal in the outer ECM ring around each cell and between cells organized into multicellular clusters (**Fig. 12C**). Quantification of the integrated intensity of nascent Gal in the ECM ring of each cell showed that nascent Gal deposition was greatest around cells in the 50G50H environment ( $p = 0.0294$  vs. 75G25H,  $p = 0.0001$  vs. 100G), though there was no significant difference between the 100G and 75G25H groups ( $p = 0.0774$ ) (**Fig. 12D**).

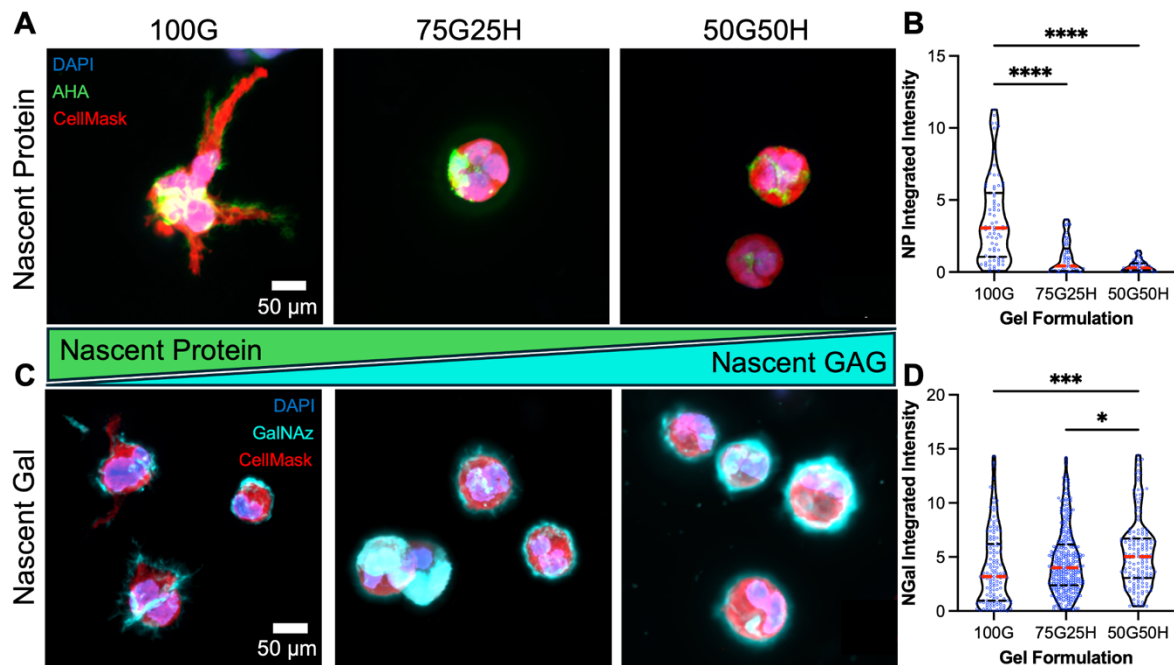


**Figure 12. Microenvironment Impact on Matrix-Producing Phenotype.** [A] Representative images and [B] quantification of Nascent Protein (NP) and [C] representative images and [D] quantification of Nascent Gal (NGal) integrated intensity per cell following t=3d culture in gels with varying compositions (G = gelatin; H = HA). n>50 cells per group, from at least 2 technical replicates. \*, \*\*\*, \*\*\*\* represent p<0.05, 0.001, 0.0001 respectively.

### Adhesion and Remodelability

By specifically altering adhesion and remodelability within PHA hydrogels through the use of functionalized RGD and MMP-cleavable peptides, differences were seen in terms of nascent GAG and nascent protein production by individual MFCs by 3 days. The High Adhesion, High Remodeling group contained cells with the greatest deposition of nascent protein ( $p < 0.0001$ ), while no difference was seen in nascent protein deposition between the No Adhesion, No Remodeling group and the High Adhesion, High Remodeling Group ( $p > 0.9999$ ) (**Fig. 13A**). However, the same effect was not observed when strictly measuring nascent Gal, with the No Adhesion, No Remodeling group containing cells with significant lower nascent Gal production compared to all other groups ( $p < 0.0001$ ). No significant differences in nascent Gal deposition were seen between the other three groups ( $p = 0.8917, 0.5063, 0.9999$ ) (**Fig. 13B**).

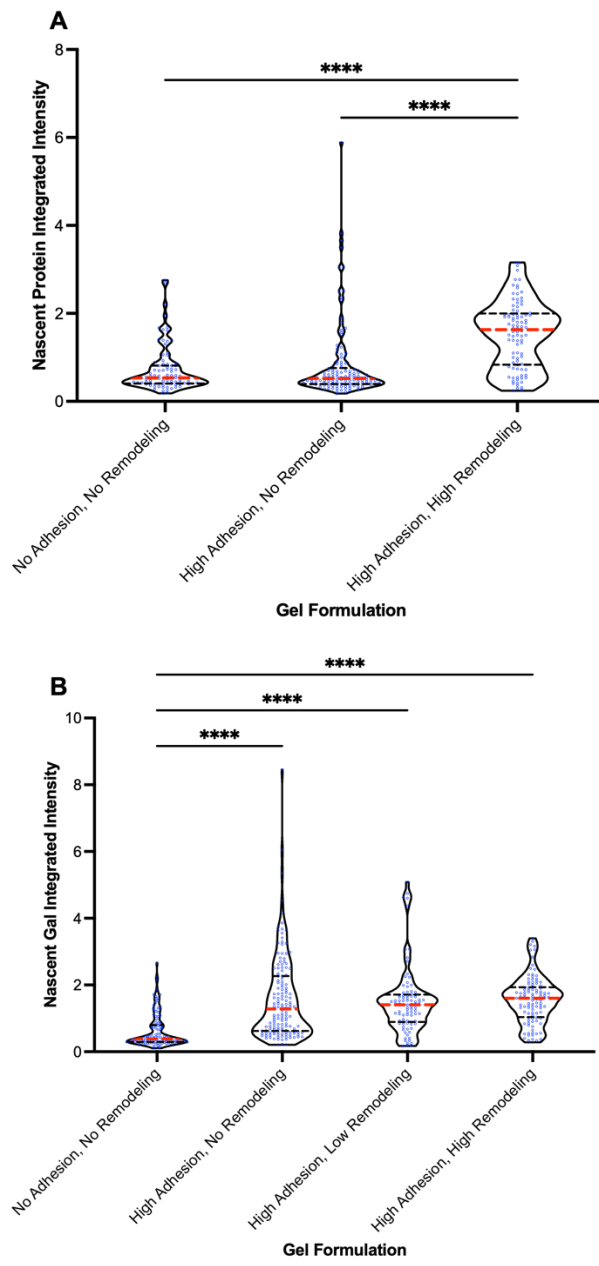


**Figure 13. Remodelability mediates Nascent Protein but not Nascent Gal deposition by MFCs.** [A] Quantification of Nascent Protein and [B] Nascent Gal integrated intensity between different groups with altered levels of adhesion and remodelability.  $n > 80$  cells per groups. \*\*\*\* represents  $p < 0.0001$

## Discussion

The design and implementation of fiber-reinforced scaffolds to replace aligned tissues like the meniscus has gained popularity in recent years<sup>13,16,18,20-23</sup>, but the cell-scale patterns of responses within these repair microenvironments is poorly understood. In this study, we investigated spatially dependent responses of single cells in these environments and the influence of fiber-reinforcement, substrate stiffness, remodelability, and adhesion on early morpho-mechanoresponses of MSCs and extracellular matrix deposition by MFCs. Our cell clustering approach identified distinct MSC sub-populations within stiff-soft microenvironments, shed new light on spatial patterns of cell response, and increased our understanding of how the interplay between microenvironment stiffness and remodeling can tune cellular response patterns in a meniscus repair microenvironment. Additionally, our matrix metabolic labeling approach allowed for the visualization of early composition and organization of nascent matrix deposition which likely correlates with long-term mature meniscal tissue properties.

Heterogeneity in MSC populations has been well documented in the field<sup>75-77</sup>. Certainly, in terms of bone-marrow derived cells, cellular subsets are present, further owing to the heterogeneity present in the raw, unsorted marrow-derived preparations in this study. From spatial data of MSC morphological response (Conformity Index) and mechanoresponse (YAP), a distance dependent correlation was observed, with response decreasing with distance from the fiber. However, the weak correlations reduced confidence in generating conclusions about patterns of cellular responsivity within the fiber-reinforced microenvironment, motivating the need to use machine learning principles, as done in other single-cell response studies<sup>52,77,78</sup>. In the present study, PCA was performed to reduce 23 cell and nuclear parameters to a lower-dimension space. A cumulative variability threshold of 80% was set prior to analysis in order to preserve most of the variability of the data set while also reducing dimensionality, resulting in five principal components being used for clustering analysis (83.78% variability). An

agglomerative hierarchical clustering approach successfully divided our heterogeneous cell population into three distinct clusters with varying levels of response (HR, MR, LR), based on conformity index and morpho-mechanoresponse. Through this clustering approach, the heterogeneous MSC population, composed of various uncharacterized cell types, as well as both senescent and non-senescent MSCs<sup>77</sup>, were divided to highlight key cell sub-groups of interest.

Upon organization of these cell clusters, we obtained an understanding of spatial patterns of cell localization in different cell groups. Hyde et al. demonstrated that cell patterning during meniscal tissue formation may mediate ECM organization<sup>36</sup>, contributing to the significance of spatial patterns seen in this study. The distance-dependent organization of more responsive cells dominating areas closer to the fiber provide insight into the spatial dynamics of the early fiber-reinforced microenvironment, which may contribute to the architecture of mature, aligned tissues<sup>28,36</sup>. The interplay between low and high response cells in terms of their localization within stiff-soft microenvironments can be crucial to optimizing fiber-reinforced technologies at the cellular level to maximize organization and alignment of eventual deposited meniscal tissue. Specifically, we have explored how the depth by which cells can sense a rigid fiber in a stiff-soft environment<sup>45,47</sup> can influence spatial patterning of the 3D fiber-reinforced microenvironment. By illustrating the distance-dependent nature by which cells spatially sense rigid material across a soft medium, we have provided insight into the dynamics of cell instruction, in terms of orientation and differentiation, by topological features of the cell-biomaterial network. These dynamics can inform meniscus scaffold design at the microscale, from fiber spacing/diameter to methods for cell encapsulation to maximize sensing.

The physical properties of the fiber-reinforced microenvironment, namely substrate stiffness and 3D matrix remodeling, can have major implications on cell matrix mechanosensing and differentiation<sup>21,33,35,37,39,44,79,80</sup>. By modulating these factors in this study, we have shown

novel evidence that, in the context of response to a stiff reinforcing polymer fiber, substrate stiffness predominantly mediates the extent to which responsive cells respond and conform (“how”), while the ability to remodel 3D matrix primarily influences the distance to which the cells can respond (“where”). The unique interplay between substrate stiffness and remodeling can be utilized to finely govern cell response in a fiber-reinforced microenvironment, controlling ultimate tissue deposition and architecture<sup>27,28,33,34,36,46</sup>. To optimize fiber-reinforced scaffold technology for anisotropic tissue regeneration<sup>26,49</sup>, the cellular nuances at the microscale and microenvironmental factors that govern these nuances must be considered<sup>37,44</sup>.

Beyond cell responses within a fiber-reinforced microenvironment, we have also shown evidence that altering the 3D biomaterial composition surrounding MFCs can precisely instruct cellular processes such as mechanoreponse and matrix deposition. This finding can guide tissue engineering approaches to finely pattern and meniscus scaffold aiming to maintain the ultrastructural heterogeneity of the native meniscus<sup>59</sup>. We have shown differences in cellular morphology between inner and outer meniscus cells in the native rabbit meniscus, which may point to differences in eventual gene expression and matrix production profiles<sup>81-83</sup>. However, there is considerable cellular heterogeneity within both the outer and inner specific regions, challenging the traditional notion of distinct outer vs. inner MFCs. For example, while circumferentially oriented fibers are typically described in the outer third zone of the meniscus, we have visualized aligned collagen fibers throughout the radial axis and into the inner zone of the meniscus, the region most impacted by radial tears. In healthy tissue, cellular arrangement tracks with this collagen organization, with a large portion of nuclear aspect ratios greater than two, even at the inner. Furthermore, in the inner third of tissue, “strings” (6-12 cells) of cells align along individual collagen bundles, suggesting the inner meniscus contains cells responsible for aligned matrix. Cellular arrangement is a precursor to subsequent matrix deposition and organization both during development and in tissue regeneration<sup>28</sup>. Therefore, our data detailing

the early matrix producing capacity of the heterogenous MFC population is highly valuable to the field in understand dynamics of meniscal tissue regeneration.

Through the use of our metabolic labeling approach to visualize early nascent matrix produced by MFCs, we have furthered understanding of the matrix-depositing capabilities of MFCs cultured in various biomaterial environments. Our data showing the progression nascent protein deposition from 3-14 days demonstrating the inherent ability of the whole meniscal cell population to align and deposit aligned matrix over time, even in initially isotropic environments. This indicates that most meniscus cells communicate to form strings, suggesting that the aligned matrix-forming potential of MFCs is plastic and can be guided by the 3D biomaterial microenvironment. In addition to L-azidohomoalanine (AHA) being utilized to visualize nascent protein, N-acetylgalactosamine was replaced by N-azidoacetylgalactosamine (GalNAz) to visualize synthesized glycosaminoglycans (GAGs; chondroitin sulfate and dermatan sulfate). At 3 days of culture in GelMA alone, meniscus cell aggregates displayed protrusions and initial pericellular protein deposition. However, when methacrylated hyaluronic acid (MeHA) was introduced into gels, less protein matrix was produced per cell. Interestingly, nascent GAG deposition, predominantly in the pericellular matrix, increased with higher HA content. Thus, we demonstrate that the meniscus cell population's matrix-depositing potential is guided by early microenvironmental interactions. When culturing the cells for longer (14 days), higher initial HA content led to reduced aligned matrix deposition and directionality, suggesting that the early enhanced GAG production in the pericellular area caused by incorporation of MeHA may inhibit nascent protein deposition and thus aligned, organized matrix<sup>84</sup> that was seen in GelMA alone. While HA may cause changes in cellular behavior and chondrogenesis via CD44 interactions<sup>85,86</sup>, we attribute this inhibition of aligned matrix deposition to decreased integrin-mediated cell-matrix adhesions and reduced remodelability, due to reduced adhesion sites and enzyme degradable sequences in HA compared to gelatin. Using our pentanoate-functionalized

HA (PHA) hydrogel system with functionalized RGD (adhesion) and MMP-cleavable (remodelability) peptides, we were able to provide novel evidence for this phenomenon, with increased remodelability and adhesion in the 3D microenvironment allowing for more robust nascent ECM deposition by MFCs within 3 days.

Together, the patterns of cell response and matrix production by both MSCs and MFCs we have provided can be applied to microscale design of meniscus tissue engineering approaches optimizing early cell instruction to enhance proper tissue maturation at the macroscale through manipulation of substrate topography, fiber size/orientation, biomaterial composition and cell-matrix interactions.

The results in this study are of interest to the tissue engineering field but present some limitations. For example, while the cellular heterogeneity within our simulated fiber-reinforced microenvironment was considered, the heterogeneity of the fibrin gel and GelMA/MeHA substrates must also be acknowledged. As a common hydrogel system used in tissue engineering applications, the multiscale mechanical heterogeneity of fibrin gels has been well documented<sup>87,88</sup>. While we performed mechanical testing of overall fibrin gel formulations, heterogeneity is still present within the polymerization and crosslinking of the microscale fibrin microenvironment, which we have shown can influence the extent by which cells can respond. Second, although our clustering approach was successful in identifying responsive populations of MSCs used in our model system, the heterogeneity of cells must still be acknowledged. MSCs used in this study have not been definitively characterized, although it is reasonable to assume that only stromal cells adhered to the plastic dish during cell expansion.

## Conclusions

In this study, we utilized a variety of tissue engineering approaches to simulate a meniscus repair microenvironment in order to better understand cell-biomaterial interactions and how these interactions can be controlled by offer precise guidance of cellular response and activity. By utilizing a variety of cell types (MSCs and MFCs) and gel substrates (fibrin, GelMA, MeHA), this research has furthered our understanding of the macroscale, microscale, and nanoscale players involved in cell instruction modalities for meniscus tissue engineering. With the current lack of reliable meniscus replacements on the market, we have provided an avenue towards a regionally dependent meniscus scaffold that seeks to precisely control early cell-biomaterial and cell-matrix interactions to form an optimal replacement that fully recapitulates the micromechanical heterogeneity and overall biomechanical functions of the native meniscus in ensuring lubrication, load distribution, and overall joint stability in the knee.

## References

1. McNulty AL, Guilak F. Mechanobiology of the meniscus. *J Biomech* 2015;48(8):1469-78, doi:10.1016/j.jbiomech.2015.02.008
2. Walker PS, Erkman MJ. The role of the menisci in force transmission across the knee. *Clin Orthop Relat Res* 1975;109):184-92, doi:10.1097/00003086-197506000-00027
3. Bansal S, Floyd ER, M AK, et al. Meniscal repair: The current state and recent advances in augmentation. *J Orthop Res* 2021;39(7):1368-1382, doi:10.1002/jor.25021
4. Makris EA, Hadidi P, Athanasiou KA. The knee meniscus: structure-function, pathophysiology, current repair techniques, and prospects for regeneration. *Biomaterials* 2011;32(30):7411-31, doi:10.1016/j.biomaterials.2011.06.037
5. Fithian DC, Kelly MA, Mow VC. Material properties and structure-function relationships in the menisci. *Clin Orthop Relat Res* 1990;252):19-31
6. Adams BG, Houston MN, Cameron KL. The Epidemiology of Meniscus Injury. *Sports Med Arthrosc Rev* 2021;29(3):e24-e33, doi:10.1097/JSA.0000000000000329
7. Ozeki N, Seil R, Krych AJ, et al. Surgical treatment of complex meniscus tear and disease: state of the art. *J ISAKOS* 2021;6(1):35-45, doi:10.1136/jisakos-2019-000380
8. Merriam AR, Patel JM, Culp BM, et al. Successful Total Meniscus Reconstruction Using a Novel Fiber-Reinforced Scaffold: A 16- and 32-Week Study in an Ovine Model. *Am J Sports Med* 2015;43(10):2528-37, doi:10.1177/0363546515595065
9. Hall M, Nielsen JH, Holsgaard-Larsen A, et al. Forward lunge knee biomechanics before and after partial meniscectomy. *Knee* 2015;22(6):506-9, doi:10.1016/j.knee.2015.03.005
10. Thorlund JB, Holsgaard-Larsen A, Creaby MW, et al. Changes in knee joint load indices from before to 12 months after arthroscopic partial meniscectomy: a prospective cohort study. *Osteoarthritis Cartilage* 2016;24(7):1153-9, doi:10.1016/j.joca.2016.01.987

11. Chung KS, Ha JK, Kim YS, et al. National Trends of Meniscectomy and Meniscus Repair in Korea. *J Korean Med Sci* 2019;34(32):e206, doi:10.3346/jkms.2019.34.e206
12. Patel JM. Impediments to Meniscal Repair: Factors at Play Beyond Vascularity. *Front Bioeng Biotechnol* 2022;10(843166), doi:10.3389/fbioe.2022.843166
13. Patel JM, Brzezinski A, Ghodbane SA, et al. Personalized Fiber-Reinforcement Networks for Meniscus Reconstruction. *J Biomech Eng* 2020;142(5), doi:10.1115/1.4045402
14. Patel JM, Ghodbane SA, Brzezinski A, et al. Tissue-Engineered Total Meniscus Replacement With a Fiber-Reinforced Scaffold in a 2-Year Ovine Model. *Am J Sports Med* 2018;46(8):1844-1856, doi:10.1177/0363546517752668
15. Pucha SA, Hasson M, Solomon H, et al. Revealing Early Spatial Patterns of Cellular Responsivity in Fiber-Reinforced Microenvironments. *Tissue Engineering Part A* 2024;30(19-20):614-626, doi:10.1089/ten.tea.2024.0017
16. Pei B, Wang W, Fan Y, et al. Fiber-reinforced scaffolds in soft tissue engineering. *Regen Biomater* 2017;4(4):257-268, doi:10.1093/rb/rbx021
17. Lee CH, Rodeo SA, Fortier LA, et al. Protein-releasing polymeric scaffolds induce fibrochondrocytic differentiation of endogenous cells for knee meniscus regeneration in sheep. *Sci Transl Med* 2014;6(266):266ra171, doi:10.1126/scitranslmed.3009696
18. Sarikaya B, Gumusderelioglu M. Aligned silk fibroin/poly-3-hydroxybutyrate nanofibrous scaffolds seeded with adipose-derived stem cells for tendon tissue engineering. *Int J Biol Macromol* 2021;193(Pt A):276-286, doi:10.1016/j.ijbiomac.2021.10.104
19. Moore AC, Hennessy MG, Nogueira LP, et al. Fiber reinforced hydrated networks recapitulate the poroelastic mechanics of articular cartilage. *Acta Biomater* 2023;167(69-82), doi:10.1016/j.actbio.2023.06.015
20. Xie Y, Zhang F, Akkus O, et al. A collagen/PLA hybrid scaffold supports tendon-derived cell growth for tendon repair and regeneration. *J Biomed Mater Res B Appl Biomater* 2022;110(12):2624-2635, doi:10.1002/jbm.b.35116

21. Jordan AM, Kim SE, Van de Voorde K, et al. In Situ Fabrication of Fiber Reinforced Three-Dimensional Hydrogel Tissue Engineering Scaffolds. *ACS Biomater Sci Eng* 2017;3(8):1869-1879, doi:10.1021/acsbiomaterials.7b00229
22. Liu X, Huang C, Feng Y, et al. Reinforcement of a porous collagen scaffold with surface-activated PLA fibers. *J Biomater Sci Polym Ed* 2010;21(6-7):963-77, doi:10.1163/156856209X461034
23. Choi DJ, Choi K, Park SJ, et al. Suture Fiber Reinforcement of a 3D Printed Gelatin Scaffold for Its Potential Application in Soft Tissue Engineering. *Int J Mol Sci* 2021;22(21), doi:10.3390/ijms222111600
24. Hokugo A, Takamoto T, Tabata Y. Preparation of hybrid scaffold from fibrin and biodegradable polymer fiber. *Biomaterials* 2006;27(1):61-7, doi:10.1016/j.biomaterials.2005.05.030
25. Zaszczynska A, Moczulska-Heljak M, Gradys A, et al. Advances in 3D Printing for Tissue Engineering. *Materials (Basel)* 2021;14(12), doi:10.3390/ma14123149
26. Warren PB, Huebner P, Spang JT, et al. Engineering 3D-Bioprinted scaffolds to induce aligned extracellular matrix deposition for musculoskeletal soft tissue replacement. *Connect Tissue Res* 2017;58(3-4):342-354, doi:10.1080/03008207.2016.1276177
27. Bryant SJ, Vernerey FJ. Programmable Hydrogels for Cell Encapsulation and Neo-Tissue Growth to Enable Personalized Tissue Engineering. *Adv Healthc Mater* 2018;7(1), doi:10.1002/adhm.201700605
28. Tsinman TK, Jiang X, Han L, et al. Intrinsic and growth-mediated cell and matrix specialization during murine meniscus tissue assembly. *FASEB J* 2021;35(8):e21779, doi:10.1096/fj.202100499R
29. Gamer LW, Shi RR, Gendelman A, et al. Identification and characterization of adult mouse meniscus stem/progenitor cells. *Connect Tissue Res* 2017;58(3-4):238-245, doi:10.1080/03008207.2016.1271797

30. Gamer LW, Xiang L, Rosen V. Formation and maturation of the murine meniscus. *J Orthop Res* 2017;35(8):1683-1689, doi:10.1002/jor.23446
31. Hellio Le Graverand MP, Sciore P, Eggerer J, et al. Formation and phenotype of cell clusters in osteoarthritic meniscus. *Arthritis Rheum* 2001;44(8):1808-18, doi:10.1002/1529-0131(200108)44:8<1808::AID-ART318>3.0.CO;2-B
32. Son M, Levenston ME. Discrimination of meniscal cell phenotypes using gene expression profiles. *Eur Cell Mater* 2012;23(195-208, doi:10.22203/ecm.v023a15
33. Kumar A, Placone JK, Engler AJ. Understanding the extracellular forces that determine cell fate and maintenance. *Development* 2017;144(23):4261-4270, doi:10.1242/dev.158469
34. Nathan AS, Baker BM, Nerurkar NL, et al. Mechano-topographic modulation of stem cell nuclear shape on nanofibrous scaffolds. *Acta Biomater* 2011;7(1):57-66, doi:10.1016/j.actbio.2010.08.007
35. Rehfeldt F, Engler AJ, Eckhardt A, et al. Cell responses to the mechanochemical microenvironment--implications for regenerative medicine and drug delivery. *Adv Drug Deliv Rev* 2007;59(13):1329-39, doi:10.1016/j.addr.2007.08.007
36. Hyde G, Boot-Handford RP, Wallis GA. Col2a1 lineage tracing reveals that the meniscus of the knee joint has a complex cellular origin. *J Anat* 2008;213(5):531-8, doi:10.1111/j.1469-7580.2008.00966.x
37. Shan J, Chi Q, Wang H, et al. Mechanosensing of cells in 3D gel matrices based on natural and synthetic materials. *Cell Biol Int* 2014;38(11):1233-43, doi:10.1002/cbin.10325
38. Caliarì SR, Vega SL, Kwon M, et al. Dimensionality and spreading influence MSC YAP/TAZ signaling in hydrogel environments. *Biomaterials* 2016;103(314-323, doi:10.1016/j.biomaterials.2016.06.061
39. Saraswathibhatla A, Indana D, Chaudhuri O. Cell-extracellular matrix mechanotransduction in 3D. *Nat Rev Mol Cell Biol* 2023;24(7):495-516, doi:10.1038/s41580-023-00583-1

40. Nelson DW, Gilbert RJ. Extracellular Matrix-Mimetic Hydrogels for Treating Neural Tissue Injury: A Focus on Fibrin, Hyaluronic Acid, and Elastin-Like Polypeptide Hydrogels. *Adv Healthc Mater* 2021;10(22):e2101329, doi:10.1002/adhm.202101329
41. Snyder TN, Madhavan K, Intrator M, et al. A fibrin/hyaluronic acid hydrogel for the delivery of mesenchymal stem cells and potential for articular cartilage repair. *J Biol Eng* 2014;8(10), doi:10.1186/1754-1611-8-10
42. McDermott AM, Eastburn EA, Kelly DJ, et al. Effects of chondrogenic priming duration on mechanoregulation of engineered cartilage. *J Biomech* 2021;125(110580), doi:10.1016/j.jbiomech.2021.110580
43. Noori A, Ashrafi SJ, Vaez-Ghaemi R, et al. A review of fibrin and fibrin composites for bone tissue engineering. *Int J Nanomedicine* 2017;12(4937-4961), doi:10.2147/IJN.S124671
44. Yang B, Wei K, Loebel C, et al. Enhanced mechanosensing of cells in synthetic 3D matrix with controlled biophysical dynamics. *Nat Commun* 2021;12(1):3514, doi:10.1038/s41467-021-23120-0
45. Chen J, Chen X, Ma Y, et al. Effect of Anisotropic Structural Depth on Orientation and Differentiation Behavior of Skeletal Muscle Cells. *ACS Omega* 2023;8(44):41374-41382, doi:10.1021/acsomega.3c04981
46. Jeon O, Kim TH, Alsberg E. Reversible dynamic mechanics of hydrogels for regulation of cellular behavior. *Acta Biomater* 2021;136(88-98), doi:10.1016/j.actbio.2021.09.032
47. Buxboim A, Rajagopal K, Brown AE, et al. How deeply cells feel: methods for thin gels. *J Phys Condens Matter* 2010;22(19):194116, doi:10.1088/0953-8984/22/19/194116
48. Cho S, Irianto J, Discher DE. Mechanosensing by the nucleus: From pathways to scaling relationships. *J Cell Biol* 2017;216(2):305-315, doi:10.1083/jcb.201610042
49. Huebner P, Warren PB, Chester D, et al. Mechanical properties of tissue formed in vivo are affected by 3D-bioprinted scaffold microarchitecture and correlate with ECM collagen fiber alignment. *Connect Tissue Res* 2020;61(2):190-204, doi:10.1080/03008207.2019.1624733

50. Dupont S, Morsut L, Aragona M, et al. Role of YAP/TAZ in mechanotransduction. *Nature* 2011;474(7350):179-83, doi:10.1038/nature10137
51. Piccolo S, Dupont S, Cordenonsi M. The biology of YAP/TAZ: hippo signaling and beyond. *Physiol Rev* 2014;94(4):1287-312, doi:10.1152/physrev.00005.2014
52. Bonnevie ED, Ashinsky BG, Dekky B, et al. Cell morphology and mechanosensing can be decoupled in fibrous microenvironments and identified using artificial neural networks. *Sci Rep* 2021;11(1):5950, doi:10.1038/s41598-021-85276-5
53. Hao J, Zhang Y, Wang Y, et al. Role of extracellular matrix and YAP/TAZ in cell fate determination. *Cell Signal* 2014;26(2):186-91, doi:10.1016/j.cellsig.2013.11.006
54. Hellio Le Graverand MP, Ou Y, Schield-Yee T, et al. The cells of the rabbit meniscus: their arrangement, interrelationship, morphological variations and cytoarchitecture. *J Anat* 2001;198(Pt 5):525-35, doi:10.1046/j.1469-7580.2000.19850525.x
55. Verdonk PC, Forsyth RG, Wang J, et al. Characterisation of human knee meniscus cell phenotype. *Osteoarthritis Cartilage* 2005;13(7):548-60, doi:10.1016/j.joca.2005.01.010
56. Sanchez-Adams J, Willard VP, Athanasiou KA. Regional variation in the mechanical role of knee meniscus glycosaminoglycans. *J Appl Physiol (1985)* 2011;111(6):1590-6, doi:10.1152/jappphysiol.00848.2011
57. Bursac P, Arnoczky S, York A. Dynamic compressive behavior of human meniscus correlates with its extra-cellular matrix composition. *Biorheology* 2009;46(3):227-37, doi:10.3233/BIR-2009-0537
58. Li Q, Qu F, Han B, et al. Micromechanical anisotropy and heterogeneity of the meniscus extracellular matrix. *Acta Biomater* 2017;54(356-366), doi:10.1016/j.actbio.2017.02.043
59. McDevitt CA, Webber RJ. The ultrastructure and biochemistry of meniscal cartilage. *Clin Orthop Relat Res* 1990;252):8-18
60. Mahmood F, Clarke J, Riches P. The ionic contribution of proteoglycans to mechanical stiffness of the meniscus. *Med Eng Phys* 2019;64(23-27), doi:10.1016/j.medengphy.2018.12.010

61. Lee SH, Li Z, Zhang EY, et al. Precision Repair of Zone-Specific Meniscal Injuries Using a Tunable Extracellular Matrix-Based Hydrogel System. *bioRxiv* 2024, doi:10.1101/2024.09.12.612723
62. Zhang ZZ, Jiang D, Ding JX, et al. Role of scaffold mean pore size in meniscus regeneration. *Acta Biomater* 2016;43(314-326, doi:10.1016/j.actbio.2016.07.050
63. Ligorio C, Mata A. Synthetic extracellular matrices with function-encoding peptides. *Nat Rev Bioeng* 2023;1-19, doi:10.1038/s44222-023-00055-3
64. Lichtenberg JY, Ramamurthy E, Young AD, et al. Leader cells mechanically respond to aligned collagen architecture to direct collective migration. *PLoS One* 2024;19(1):e0296153, doi:10.1371/journal.pone.0296153
65. Legerstee K, Geverts B, Slotman JA, et al. Dynamics and distribution of paxillin, vinculin, zyxin and VASP depend on focal adhesion location and orientation. *Sci Rep* 2019;9(1):10460, doi:10.1038/s41598-019-46905-2
66. Wei L, Chen Q, Zheng Y, et al. Potential Role of Integrin alpha(5)beta(1)/Focal Adhesion Kinase (FAK) and Actin Cytoskeleton in the Mechanotransduction and Response of Human Gingival Fibroblasts Cultured on a 3-Dimension Lactide-Co-Glycolide (3D PLGA) Scaffold. *Med Sci Monit* 2020;26(e921626, doi:10.12659/MSM.921626
67. Das SL, Bose P, Lejeune E, et al. Extracellular Matrix Alignment Directs Provisional Matrix Assembly and Three Dimensional Fibrous Tissue Closure. *Tissue Eng Part A* 2021;27(23-24):1447-1457, doi:10.1089/ten.tea.2020.0332
68. Barker TH, Engler AJ. The provisional matrix: setting the stage for tissue repair outcomes. *Matrix Biol* 2017;60-61(1-4, doi:10.1016/j.matbio.2017.04.003
69. Rothrauff BB, Shimomura K, Gottardi R, et al. Anatomical region-dependent enhancement of 3-dimensional chondrogenic differentiation of human mesenchymal stem cells by soluble meniscus extracellular matrix. *Acta Biomater* 2017;49(140-151, doi:10.1016/j.actbio.2016.11.046

70. Stirling DR, Swain-Bowden MJ, Lucas AM, et al. CellProfiler 4: improvements in speed, utility and usability. *Bmc Bioinformatics* 2021;22(1), doi:ARTN 433  
10.1186/s12859-021-04344-9
71. Zhao QP, Xu MT, Fränti P. Sum-of-Squares Based Cluster Validity Index and Significance Analysis. *Lect Notes Comput Sc* 2009;5495(313-322)
72. Hartigan JA. Clustering algorithms. Wiley: New York,; 1975.
73. Loebel C, Kwon MY, Wang C, et al. Metabolic Labeling to Probe the Spatiotemporal Accumulation of Matrix at the Chondrocyte-Hydrogel Interface. *Adv Funct Mater* 2020;30(44), doi:10.1002/adfm.201909802
74. Loebel C, Saleh AM, Jacobson KR, et al. Metabolic labeling of secreted matrix to investigate cell-material interactions in tissue engineering and mechanobiology. *Nat Protoc* 2022;17(3):618-648, doi:10.1038/s41596-021-00652-9
75. Costa LA, Eiro N, Fraile M, et al. Functional heterogeneity of mesenchymal stem cells from natural niches to culture conditions: implications for further clinical uses. *Cell Mol Life Sci* 2021;78(2):447-467, doi:10.1007/s00018-020-03600-0
76. Ho AD, Wagner W, Franke W. Heterogeneity of mesenchymal stromal cell preparations. *Cytotherapy* 2008;10(4):320-30, doi:10.1080/14653240802217011
77. Weber L, Lee BS, Imboden S, et al. Phenotyping senescent mesenchymal stromal cells using AI image translation. *Curr Res Biotechnol* 2023;5(doi:10.1016/j.crbiot.2023.100120)
78. Chen D, Sarkar S, Candia J, et al. Machine learning based methodology to identify cell shape phenotypes associated with microenvironmental cues. *Biomaterials* 2016;104(104-18), doi:10.1016/j.biomaterials.2016.06.040
79. Discher DE, Janmey P, Wang YL. Tissue cells feel and respond to the stiffness of their substrate. *Science* 2005;310(5751):1139-43, doi:10.1126/science.1116995

80. Nahum A, Koren Y, Ergaz B, et al. Inference of long-range cell-cell force transmission from ECM remodeling fluctuations. *Commun Biol* 2023;6(1):811, doi:10.1038/s42003-023-05179-1
81. Baker BM, Gee AO, Sheth NP, et al. Meniscus tissue engineering on the nanoscale: from basic principles to clinical application. *J Knee Surg* 2009;22(1):45-59, doi:10.1055/s-0030-1247727
82. Baker BM, Nathan AS, Huffman GR, et al. Tissue engineering with meniscus cells derived from surgical debris. *Osteoarthritis Cartilage* 2009;17(3):336-45, doi:10.1016/j.joca.2008.08.001
83. Mauck RL, Martinez-Diaz GJ, Yuan X, et al. Regional multilineage differentiation potential of meniscal fibrochondrocytes: implications for meniscus repair. *Anat Rec (Hoboken)* 2007;290(1):48-58, doi:10.1002/ar.20419
84. McCorry MC, Kim J, Springer NL, et al. Regulation of proteoglycan production by varying glucose concentrations controls fiber formation in tissue engineered menisci. *Acta Biomater* 2019;100(173-183), doi:10.1016/j.actbio.2019.09.026
85. Kim Y, Kumar S. CD44-mediated adhesion to hyaluronic acid contributes to mechanosensing and invasive motility. *Mol Cancer Res* 2014;12(10):1416-29, doi:10.1158/1541-7786.MCR-13-0629
86. Wu SC, Chen CH, Chang JK, et al. Hyaluronan initiates chondrogenesis mainly via CD44 in human adipose-derived stem cells. *J Appl Physiol (1985)* 2013;114(11):1610-8, doi:10.1152/jappphysiol.01132.2012
87. Fogelson AL, Nelson AC, Zapata-Allegro C, et al. Development of Fibrin Branch Structure before and after Gelation. *SIAM J Appl Math* 2022;82(1):267-293, doi:10.1137/21m1401024

88. Jimenez JM, Tuttle T, Guo Y, et al. Multiscale mechanical characterization and computational modeling of fibrin gels. *Acta Biomater* 2023;162(292-303, doi:10.1016/j.actbio.2023.03.026